

1 **Single Nucleus Multiomic Profiling Reveals Age-Dynamic Regulation** 2 **of Host Genes Associated with SARS-CoV-2 Infection**

3
4
5 Allen Wang^{1#*}, Joshua Chiou^{2#}, Olivier B Poirion^{1#}, Justin Buchanan^{1#}, Michael J
6 Valdez^{2#}, Jamie M Verheyden³, Xiaomeng Hou¹, Minzhe Guo^{4,5}, Jacklyn M Newsome³,
7 Parul Kudtarkar³, Dina A Faddah⁶, Kai Zhang⁷, Randee E Young^{3,8}, Justinn Barr³,
8 Ravi Misra⁹, Heidie Huyck⁹, Lisa Rogers⁹, Cory Poole⁹,
9 Jeffery A. Whitsett⁴, Gloria Pryhuber⁹, Yan Xu^{4,5},
10 Kyle J Gaulton^{3*}, Sebastian Preissl^{1*}, Xin Sun^{3,10*} and NHLBI LungMap Consortium

11
12
13 ¹Center for Epigenomics & Department of Cellular & Molecular Medicine, University of
14 California, San Diego, La Jolla, CA 92093

15
16 ²Biomedical Sciences Graduate Program, University of California San Diego, La Jolla,
17 CA, 92093

18
19 ³Department of Pediatrics, University of California-San Diego, La Jolla, CA 92093

20
21 ⁴Division of Neonatology, Perinatal and Pulmonary Biology, Cincinnati Children's
22 Hospital Medical Center, Cincinnati, OH 45267

23
24 ⁵Department of Pediatrics, College of Medicine, University of Cincinnati, Cincinnati, OH
25 45267

26
27 ⁶Vertex Pharmaceuticals, 3215 Merryfield Rd., San Diego CA, 92121

28
29 ⁷Ludwig Institute for Cancer Research, La Jolla, CA 92093

30
31 ⁸Laboratory of Genetics, Department of Medical Genetics, University of Wisconsin-
32 Madison, Madison, WI 53706.

33
34 ⁹Department of Pediatrics and Clinical & Translational Science Institute, University of
35 Rochester Medical Center

36
37 ¹⁰Department of Biological Sciences, University of California-San Diego, La Jolla, CA
38 92093.

39
40
41
42
43 #Authors contributed equally to this work.

47 Corresponding Authors*: Xin Sun (Lead contact)
48 xinsun@ucsd.edu
49
50 Sebastian Preissl
51 spreissl@health.ucsd.edu
52
53 Kyle J Gaulton
54 kgaulton@health.ucsd.edu
55
56 Allen Wang
57 a5wang@health.ucsd.edu

58 **SUMMARY**

59 Respiratory failure is the leading cause of COVID-19 death and disproportionately
60 impacts adults more than children. Here, we present a large-scale snATAC-seq dataset
61 (90,980 nuclei) of the human lung, generated in parallel with snRNA-seq (46,500 nuclei),
62 from healthy donors of ~30 weeks, ~3 years and ~30 years of age. Focusing on genes
63 implicated in SARS-CoV-2 cell entry, we observed an increase in the proportion of
64 alveolar epithelial cells expressing *ACE2* and *TMPRSS2* in adult compared to young
65 lungs. Consistent with expression dynamics, 10 chromatin peaks linked to *TMPRSS2*
66 exhibited significantly increased activity with age and harbored IRF and STAT binding
67 sites. Furthermore, we identified 14 common sequence variants in age-increasing peaks
68 with predicted regulatory function, including several associated with respiratory traits and
69 *TMPRSS2* expression. Our findings reveal a plausible contributor to why children are
70 more resistant to COVID-19 and provide an epigenomic basis for transferring this
71 resistance to older populations.

72

73

74

75 **Keywords:**

76 COVID-19, lung, SARS-CoV-2, single cell ATAC-seq, single cell RNA-seq, age dynamics,
77 *ACE2*, *TMPRSS2*, human sequence variants, interferon signaling pathway.

78 INTRODUCTION

79 Aside from fulfilling gas-exchange functions that are vital for survival beginning with
80 the first breath, the lung functions as a critical barrier to protect against inhaled pathogens
81 such as viruses. As the COVID-19 pandemic swept across the world, the lung came into
82 focus because acute respiratory distress (ARDS) is the primary cause of mortality. Thus,
83 understanding how SARS-CoV-2 infects and impacts the lung has become an urgent call-
84 to-action.

85 The lung is composed of an elaborate airway tree that conducts air to and from the
86 distal gas-exchange units called the alveoli. In an average human adult lung, an estimated
87 480 million alveoli give rise to approximately 1,000 ft² of gas-exchange surface area
88 (Ochs et al., 2004). Airway and alveolar epithelium constitute the respiratory barrier that
89 is exposed to inhaled pathogens. Respiratory epithelial cells are thereby at the frontline
90 of infection, although pathogens that have bypassed the barrier can infect other cell types.
91 The human airway epithelium is composed of luminal cells and basal cells. Luminal cells
92 include club cells and goblet cells that moisturize the air and trap pathogens, as well as
93 ciliated cells that sweep out inhaled particles. These luminal cells are underlined by basal
94 cells, which serve as progenitors when luminal cells are lost after infection. The alveolar
95 epithelium is composed of alveolar type 1 cells (AT1s) which line the gas-blood interface
96 and alveolar type 2 cells (AT2s) which produce surfactant to reduce surface tension and
97 protect against pathogens. While SARS-CoV-2 likely infects both the airway and alveolar
98 regions of the lung, it is the damage to the alveolar region that underlines acute respiratory
99 distress syndrome (Du et al., 2020).

100 Several large scale studies including efforts from LungMap and the Human Cell Atlas
101 aim to generate a map of cell types in the human lung with single cell transcriptomics as
102 the central modality (Reyfman et al., 2019; Schiller et al., 2019; Travaglini et al., 2020; Xu
103 et al., 2016). Regions of the human genome, such as promoters or distal enhancers, can
104 regulate cell-type specific gene expression in *cis* (Consortium, 2012; Roadmap
105 Epigenomics et al., 2015; Thurman et al., 2012). Accessible or ‘open’ chromatin is a
106 hallmark of *cis*-regulatory elements, and can be assayed using techniques such as
107 DNase-seq and ATAC-seq (Buenrostro et al., 2013; Thurman et al., 2012). To overcome
108 tissue heterogeneity single cell technologies like single cell ATAC-seq have been

109 developed to map the epigenome and gene regulatory programs in component cell types
110 within heterogeneous tissues (Buenrostro et al., 2015; Chen et al., 2018; Cusanovich et
111 al., 2015; Cusanovich et al., 2018; Lareau et al., 2019; Satpathy et al., 2019). Profiles
112 derived from single cells can elucidate cell type-specific *cis*-regulatory elements,
113 transcriptional regulators driving element activity, and predicted target genes of distal
114 elements using single cell co-accessibility (Cusanovich et al., 2018; Lareau et al., 2019;
115 Pliner et al., 2018; Preissl et al., 2018; Satpathy et al., 2019). Human sequence variants
116 affecting susceptibility to complex physiological and disease traits are enriched in non-
117 coding sequence (Maurano et al., 2015; Pickrell, 2014), and cell type-specific profiles
118 derived from single cell epigenomic data can help prioritize cell types of action for these
119 variants (Chiou et al., 2019; Corces et al., 2020).

120 Both *in silico* structural modeling as well as biochemical assays have implicated
121 several key host proteins at the top of the hierarchy for SARS-CoV-2 infection. ACE2 has
122 been demonstrated as the receptor for not only the original SARS-CoV, but also SARS-
123 CoV-2 (Lan et al., 2020; Yan et al., 2020). Based mainly on literature from the original
124 SARS-CoV as well as emerging data from SARS-CoV-2 (Huang et al., 2006; Matsuyama
125 et al., 2020; Reinke et al., 2017; Walls et al., 2020; Zhou et al., 2016), TMPRSS2 and
126 CTSL are responsible for fusion of the virus with host cell by cleaving the viral Spike
127 protein. BSG is a receptor that can bind to the SARS-CoV spike protein (Chen et al.,
128 2005) and SARS-CoV-2 contains a novel cleavage site for the protease Furin, adding
129 both genes to the list of host machinery hijacked by the virus (Coutard et al., 2020;
130 Walls et al., 2020). In this study, we will focus on the genes encoding these 5 proteins,
131 *ACE2*, *TMPRSS2*, *CTSL*, *BSG*, and *FURIN*, and determine their expression and
132 associated epigenomic landscape at single cell resolution in the non-diseased human
133 lung.

134 In the race to control the COVID-19 pandemic, there has been a tremendous collective
135 effort from the research community to elucidate the mechanism underlying SARS-CoV-2
136 infection. Our study contributes to this effort through a unique dataset profiling the human
137 lung. First, we generated single cell data across neonatal, pediatric, and adult lungs from
138 three donors in each group. These data allowed us to assess age-associated changes
139 with minimal technical variation. Second, from each lung sample, we generated parallel

140 snRNA-seq and snATAC-seq data. This combination allowed us to associate cell type-
141 specific accessible chromatin profiles that may act as *cis*-regulatory regions that control
142 cell-type specific gene expression. Using these data, we first addressed cell-type
143 specificity and temporal dynamics of *ACE2*, *TMPRSS2*, *CTSL*, *BSG*, and *FURIN*
144 expression. We next identified candidate *cis*-regulatory elements co-accessible with the
145 promoters of these genes and characterized their cell-type specificity and temporal
146 dynamics. Finally, we profiled sequence variation that may impact *cis*-regulatory element
147 activity and contribute to differential susceptibility to SARS-CoV-2 infection.

148 Emerging epidemiology data, including on US cases reported by the CDC,
149 demonstrate that many fewer children tested positive for SARS-CoV-2 infection, and
150 those who tested positive generally show less severe symptoms than adults or elderly
151 individuals (Bi et al., 2020; CDC, 2020). This age divide coincides with the finding that
152 normal lung development in humans continues until the early 20s (Narayanan et al.,
153 2012). Therefore COVID-19 preferentially impacts fully mature lungs relative to
154 developing lungs. Widespread speculation has attempted to explain these age-
155 associated differences, including immune senescence in the aging population. Defining
156 the mechanism underlying the apparent resistance of children to COVID-19 will inform
157 how we can transfer this resistance to adult and elderly populations.

158

159

160 **RESULTS**

161

162 **Single nucleus RNA-seq and ATAC-seq data generation**

163 To profile cell type specific gene expression and accessible chromatin dynamics in
164 the human lung, we performed single nucleus RNA-seq (snRNA-seq) and single nucleus
165 ATAC-seq (snATAC-seq) of non-diseased human lung tissue from donors of three age
166 groups: ~30 week old gestational age (GA, prematurely born, 30wk^{GA}), ~3 year old (3yo),
167 and ~30 year old (30yo) (Supplementary Table 1). Three lungs were sampled for each
168 age group, with both males and females represented (Supplementary Table 1). Of the 9
169 donors, 5 were Caucasian, 1 was African American and 3 were of unknown ancestry. For
170 all samples, flash frozen biopsies from equivalent small airway regions of the lung were

171 used. Nuclei were isolated from individual biopsies and split into two pools, one for
172 snRNA-seq and one for snATAC-seq. For snATAC-seq, we generated technical
173 replicates for one of the 3yo donors (D032) and an additional dataset for a lung sample
174 from a 4-month-old donor (Supplementary Table 1).

175 To generate snRNA-seq libraries, we used the droplet-based Chromium Single Cell
176 3' solution (10x Genomics) (Zheng et al., 2017). The datasets showed a clear separation
177 of nuclei from background in the knee plot (Figure S1A). The average number of nuclei
178 that passed initial quality control filtering per sample was 6,676 for 30wk^{GA}, 7,379 for 3yo,
179 and 4,217 for 30yo (Figure S1B). Since we profiled nuclei with a high fraction of nascent,
180 unspliced RNA molecules, sequencing reads were mapped to an exon+intron reference.
181 We detected on average 1,662 gene/nuclei for 30wk^{GA}, 1,394 for 3yo and 1,260 for 30yo
182 (Figure S1C). Libraries were sequenced to comparable saturation (58.4 % for 30wk^{GA},
183 51.6 % for 3yo and 55.0 % for 30yo; Fig. S1D).

184 For snATAC-seq library generation we used a semi-automated combinatorial
185 barcoding platform (Cusanovich et al., 2015; Fang et al., 2019; Preissl et al., 2018) . For
186 each dataset, nuclei with >1,000 uniquely mapped sequencing reads were included in the
187 analysis (Fig. S1E). The average number of nuclei that passed this threshold per age
188 group was 8,691 for 30wk^{GA}, 7,877 for 3yo and 8,034 for 30yo (Fig. S1F). The average
189 number of reads per nucleus was 6,399 for 30wk^{GA}, 7,199 for 3yo and 8,362 for 30yo
190 (Fig. S1G). The fraction of reads in peaks (FRiP) on average per data set was 52.8 % for
191 30wk^{GA}, 54.4 % for 3yo and 45.6 % for 30yo (Fig. S1H). These values indicate
192 consistently high signal to noise ratios for all libraries.

193

194 **Age-linked increase in host genes for SARS-CoV-2 entry**

195 In total, 46,500 single nucleus transcriptomes were included in the analysis after
196 filtering out low quality nuclei and potential barcode collisions (Figure S1, Supplementary
197 Table 2, see **Methods**). Following batch correction all datasets were merged, and 31
198 clusters were identified (Figure 1A). These clusters represented all major cell types in the
199 small airway region of the lung, as well as rare cell types such as pulmonary
200 neuroendocrine cells (Figure 1A, Figure S2A, Supplementary Table 2). We identified
201 14,527 epithelial cells (31.2 % of all nuclei) in our snRNA-seq dataset. This optimal

202 representation and large number of cells allowed us power to profile gene expression
203 patterns of viral entry genes in lung epithelial cells. For downstream analysis, we excluded
204 an unclassified cluster, and enucleated erythrocytes because the latter were only
205 detected in a single neonatal sample, consistent with immaturity (Figure 1A).

206 Focusing on SARS-CoV-2 viral entry genes, we found that *ACE2* transcript was
207 detected in very few nuclei (total 80 nuclei) in the normal lung and these nuclei were
208 enriched within the epithelial lineage (Figure 1B, Supplementary Table 2). Alveolar type
209 2 (AT2) cells had the highest number of *ACE2*⁺ nuclei, accounting for 48.8% of all *ACE2*-
210 expressing nuclei (39 out of total 80 *ACE2*⁺ nuclei). In comparison, *TMPRSS2* transcript
211 was detected more frequently (e.g. in 3,315/7,226 nuclei, or 45.8% of the AT2 cells,
212 Figure 1C, Supplementary Table 2). Most *TMPRSS2*-expressing cells were epithelial
213 cells including alveolar type 1 and 2 (AT1, AT2) cells and airway cells such as club,
214 ciliated and goblet cells (Figure 1C, Supplementary Table 2). We also detected significant
215 correlation between the fraction of *ACE2*⁺ and *TMPRSS2*⁺ AT2 nuclei (Figure S2E) and
216 found 21 of the 39 *ACE*⁺ AT2 cells also expressed *TMPRSS2* (Supplementary Table 2).
217 The other three candidate genes of SARS-CoV-2 host cell entry *CTSL*, *BSG* and *FURIN*
218 were expressed in a large number of AT1, AT2, matrix fibroblast, and M1 macrophage
219 cells, as well as a small number of additional cell types (Figure S2B-D, Supplementary
220 Table 2). These findings suggest that among cells that constitute the barrier exposed to
221 inhaled pathogens, cell types in both the airway and alveolar epithelium express genes
222 critical for SARS-CoV-2 entry.

223 We next asked if there were genes enriched in *ACE2*⁺ AT2 cells as compared to *ACE2*⁻
224 AT2 cells to identify potentially co-expressed genes. Among genes that showed a trend
225 for higher expression in *ACE2*⁺ compared to *ACE2*⁻ cells was *IFNGR1* (\log_2 (fold change)
226 = 0.4, $-\log_{10}$ (p-value)=5.0; FDR corrected p=0.257, Supplementary Table 3), raising the
227 possibility that *ACE2* may be co-regulated with interferon pathway genes, in line with
228 conclusions of a recent study (Ziegler, 2020). In our data generated from normal lungs
229 this correlation was modest, suggesting there is low baseline co-expression of *ACE2* and
230 *IFNGR1*. Among genes with increased expression in *TMPRSS2*⁺ versus *TMPRSS2*⁻ AT2
231 cells was *ICAM1* (\log_2 (fold change)=0.27, $-\log_{10}$ (FDR corrected p)=12.2, Supplementary
232 Table 3), which encodes a receptor for Rhinovirus (Zhou et al., 2017). The potential co-

233 expression of *TMPRSS2* and *ICAM1* may contribute to the often-observed co-infection
234 by more than one respiratory virus. Indeed, co-infection of SARS-CoV-2 and other viruses
235 including Rhinovirus has been observed, promoting urgent calls to halt the clinical
236 practice of using positive test for other respiratory viruses as an indicator for the absence
237 of coronavirus infection (Wang et al., 2020; Wu et al., 2020). To gain additional insight
238 into the potential mechanisms of co-infection, we interrogated the expression of a number
239 of known factors, receptors and proteases that have been implicated in viral entry for
240 several key respiratory viruses (Figure S3)(Battles and McLellan, 2019; Bochkov and
241 Gern, 2016; Laporte and Naesens, 2017; Peck et al., 2015). For examples, consistent
242 with prior findings, we found that *CDHR3*, a receptor for Rhinovirus C, was expressed
243 most abundantly in ciliated cells (Battles and McLellan, 2019; Bochkov and Gern, 2016;
244 Laporte and Naesens, 2017; Peck et al., 2015). *ANPEP*, the entry receptor for HCoV-
245 229E, was predominantly expressed in macrophages and to a lesser extent in club and
246 other epithelial cells (Waradon Sungnak, 2020; Yeager et al., 1992). Compared to *ACE2*,
247 *DPP4*, which encodes the host receptor for MERS-CoV, was detected much more
248 frequently overall, and especially in AT2, AT1 and T cells (Figure S3) (Raj et al., 2013;
249 Waradon Sungnak, 2020). This single cell resolved view may contribute to a
250 comprehensive map of the routes of respiratory viral entry.

251 The leading cause of death for COVID-19 is Acute Respiratory Distress Syndrome
252 (ARDS) which is characterized by failure of gas-exchange due to destruction of the
253 alveolar region of the lung (Du et al., 2020). AT2 is an abundant epithelial cell type in the
254 alveolar region and expresses all of the SARS-CoV-2 viral entry genes assayed here and
255 likely bears the brunt of infection. Consequently, we focused on AT2 cells for follow up
256 analysis. We found that the percentage of AT2 cells expressing *ACE2* had an increasing
257 trend in 30yo adult samples compared to 3yo samples (Figure 1D). In addition, we found
258 a strong trend of increase in the percentage of AT2 cells expressing *TMPRSS2* in adult
259 samples compared to 3yo samples ($41.2 \pm 6.6\%$ for 3yo and $57.4 \pm 7.7\%$ for 30yo, $p =$
260 0.05 (t-test), Figure 1E). While very few *ACE2*⁺/*TMPRSS2*⁺ double positive AT2 nuclei
261 were detected, the fraction of these nuclei in all AT2s increased with age (0.2 % (6 nuclei)
262 in 30wk^{GA}, 0.3% (5 nuclei) in 3yo and 0.5% (10 nuclei) in 30yo, Supplementary Table 2).
263 Of note, one of the samples in the 30wk^{GA} cohort D062 appeared to be an outlier in its

264 expression of multiple analyzed genes. A review of pathology notes revealed mild
265 features of respiratory distress syndrome including epithelial autolysis and increased
266 alveolar macrophages in this sample, suggesting potential reasons for the variation. In a
267 supplementary analysis, excluding this sample resulted in stronger age-associated
268 effects (Figure S2F, G). For example, there was a significant increase in the fraction of
269 *TMPRSS2*⁺ AT2 cells between 30wk^{GA} and 30yo samples (Figure S2G).

270 The increase in proportion of AT2 cells expressing *ACE2* and *TMPRSS2* is unlikely
271 due to differences in genes captured per nucleus as the adult samples had the lowest
272 numbers of genes/nucleus, suggesting that the extent of expression increase is likely a
273 conservative estimation (Figure S1C). In contrast to the percentage of AT2 nuclei
274 expressing these genes, the expression levels per nucleus were not different across
275 different age groups for either *ACE2* (no nucleus had >1 UMI detected) or *TMPRSS2*
276 (Figure 1F). Together, an increased proportion of host cells expressed *TMPRSS2* and
277 *ACE2* in adults, the latter just a trend due to the sparsity of *ACE2*⁺ cells, suggesting that
278 a higher percentage of cells in the adult lung can be infected by SARS-CoV-2.

279 Since a large proportion of COVID-19 patients are elderly, we sought to compare viral
280 entry gene expression in aged lungs to expression in our samples. The LungMap Human
281 Tissue Core, which provided the frozen biopsies for this study, does not have donors
282 older than ~30. We therefore instead, identified 4 publicly available scRNA-seq datasets
283 from non-diseased lungs of ages >55 that served as controls in pulmonary fibrosis studies
284 (Morse et al., 2019; Reyfman et al., 2019). We integrated snRNA-seq data from our study
285 (n=9) with these 4 scRNA-seq samples (Supplementary Table 1) using Seurat 3 (Stuart
286 et al., 2019). AT2 cells clustered together across all samples with minimal evidence for
287 batch effects (Figure S4A). Compared to 30yo samples, we observed a trend for
288 increased frequency of *ACE2*⁺ ($p = 0.095$) and *TMPRSS2*⁺ ($p = 0.070$) AT2 cells in
289 the >55yo group (Aged; Figure S4B). While these patterns are consistent with
290 epidemiological findings that elderly are at highest risk, we make these observations
291 cautiously due to the multiple potential confounding variables present when comparing
292 across independent datasets spanning multiple methodologies.

293

294 **Annotation of *cis*-regulatory sequences linked to SARS-CoV-2 viral entry gene** 295 **activity**

296 To investigate *cis*-regulatory elements driving cell-type specific and age-related
297 patterns of SARS-CoV-2 viral entry gene expression, we examined snATAC-seq data
298 generated from the same nuclei preparations. After batch correction and filtering of low-
299 quality nuclei and likely doublets, we clustered and analyzed a total of 90,980 single
300 nucleus accessible chromatin profiles. We identified 19 clusters representing epithelial
301 (AT2, AT2, club, ciliated, basal and neuroendocrine), mesenchymal (myofibroblast,
302 pericyte, matrix fibroblast 1 and matrix fibroblast 2), endothelial (arterial, lymphatic, and
303 2 clusters of capillaries), and hematopoietic cell types (macrophage, B-cell, T-cell, NK cell
304 and enucleated erythrocyte) (Figure 2A). Supporting these cluster annotations, we
305 observed cell type-specific patterns of chromatin accessibility at known marker genes for
306 each cell type (Figure S5A).

307 Focusing on SARS-Cov-2 viral entry genes, both *ACE2* and *TMPRSS2* were primarily
308 accessible throughout their gene body in alveolar cells such as AT1, AT2, and airway
309 cells such as club, ciliated, and basal cells (Figure 2B). Conversely, the *CTSL* gene body
310 exhibited chromatin accessibility across epithelial cells, mesenchymal cells, endothelial,
311 and macrophages. *BSG* and *FURIN* also showed broad chromatin accessibility patterns
312 with the highest activity in endothelial cells, such as capillaries (Figure 2B). Overall, the
313 patterns of chromatin accessibility across cell types at genes involved in SARS-CoV-2
314 cell entry substantiate our conclusions from snRNA-seq data, including the finding that
315 *ACE2* and *TMPRSS2* are primarily expressed in alveolar and airway cells (Figure 1B,C).

316 To identify specific *cis*-regulatory elements that might control cell type-restricted
317 expression of the SARS-CoV-2 viral entry genes in the lung, we aggregated cells within
318 each cell type and called accessible chromatin sites from the aggregated profiles using
319 MACS2 (Zhang et al., 2008). We then identified sites mapping within 650kb of each
320 SARS-CoV-2 viral entry gene, and further identified sites that were co-accessible with the
321 gene promoter using Cicero (Pliner et al., 2018). At the *ACE2* locus, we identified 165
322 accessible chromatin sites mapping within the ± 650 kb window (Figure 2C,
323 Supplementary Table 4). Of these 165 sites, only two were co-accessible with the *ACE2*
324 promoter (Figure 2C, Supplementary Table 5). We speculate that the low number of co-

325 accessible sites is likely due to the small percentage of *ACE2*⁺ nuclei (Figure 1B). When
326 examining the accessibility of the 165 peaks at the *ACE2* locus across cell types, we
327 observed clear sub-groupings of sites, including those specific to basal cells, specific to
328 ciliated cells, and shared across basal, ciliated, AT1, AT2, and club cells (Figure 2C,
329 Supplementary Table 5).

330 At the *TMPRSS2* locus, we identified 289 accessible chromatin sites mapping in the
331 ± 650 kb window, of which 37 were co-accessible with the *TMPRSS2* promoter (Figure 2D,
332 Supplementary Tables 4 and 5). In agreement with *TMPRSS2* gene accessibility in
333 alveolar and airway cells, 113 out of the 289 elements exhibited patterns of accessibility
334 specific to basal, ciliated, club, AT1, and AT2 cells. We observed a basal cell-specific
335 cluster and two broader epithelial cell clusters (basal, ciliated, and club enriched; and
336 club, AT1, and AT2 enriched) (Figure 2D, Supplementary Table 5). Notably, the majority
337 of sites co-accessible with *TMPRSS2* (25/37) were found within these broad alveolar- and
338 airway-enriched clusters suggesting that these elements are likely responsible for
339 alveolar and airway expression of *TMPRSS2*.

340 Finally, at the *CTSL*, *FURIN*, and *BSG* loci we identified 262, 293, and 272 accessible
341 chromatin sites, respectively, within a ± 650 kb window of which 6, 56, and 47 were co-
342 accessible with their respective gene promoters (Figure S5B, C, D, Supplementary
343 Tables 4 and 5). Sites for all three genes exhibited broad patterns of accessible chromatin
344 signal across cell types consistent with broad accessibility across gene bodies. This
345 collection of cell-type resolved candidate *cis*-regulatory elements associated with SARS-
346 CoV-2 host genes will be critically important for follow up studies to determine how host
347 cell genes are regulated and how genetic variation within these elements contributes to
348 infection rate and disease outcomes.

349
350 ***Cis*-regulatory elements linked to *TPMRSS2* are part of an age-related regulatory**
351 **program associated with immune signaling in AT2 cells**

352 Having observed increasing percentages of *TMPRSS2* expressing cells with age in
353 AT2 cells (Figure 1E, Figure S2G), we speculated that *TMPRSS2* may be under the
354 control of an age-related *cis* regulatory program. To investigate whether an age-
355 associated *cis*-regulatory network exists in AT2 cells, we identified accessible chromatin

356 sites in AT2 cells that show dynamic accessibility across donor age groups. Based on our
357 findings from snRNA-seq we speculate that these dynamics will be at least in part due to
358 a higher number of cells expressing these genes rather than more activity within a cell.
359 We tested all possible pairwise age comparisons between AT2 signal from each of the
360 three groups of 30wk^{GA}, 3yo, and 30yo donors while accounting for donor to donor
361 variability (Figure 3A). Overall, we identified 22,745 age-linked sites in AT2 cells which
362 exhibited significant differences (FDR<0.05) in any pairwise comparison (Figure 3A, B).
363 Clustering of these dynamic peaks revealed five predominant groups of age-dependent
364 chromatin accessibility patterns (cl-cV, Fig 3B).

365 We identified two clusters of AT2 sites exhibiting increasing accessibility with age
366 including several sites at candidate genes for SARS-CoV-2 host genes (cIII 30yo enriched
367 and cIV 3yo + 30yo) (Figure 3B, Figure S6A, B). Intriguingly, these two clusters were
368 enriched for processes related to viral infection and immune response such as viral
369 release from host cell, interferon-gamma mediated signaling pathway, and positive
370 regulation of ERBB signaling pathway (Figure 3C, Supplementary Table 6). Also, these
371 age-dependent clusters were also enriched for phenotypes substantiated in mouse
372 studies, such as pulmonary epithelial necrosis, increased monocyte cell number, and
373 chronic inflammation (Fig. 3C, Supplementary Table 6). Further supporting an immune
374 association with age-related chromatin accessibility in AT2 cells, we observed an
375 enrichment of sequence motifs within these clusters for transcription factors involved in
376 immune signaling such as STAT, IRF, and FOS/JUN (Figure 3D, Supplementary Table
377 7).

378 We focused on the *TMPRSS2* locus and determined how many of the 37 accessible
379 chromatin sites co-accessible with the *TMPRSS2* promoter (in Figure 2D) showed
380 increased accessibility with age in AT2 cells. We identified 13 sites with age-increased
381 accessibility, of which 10 had significant effects (FDR < 0.05 via EdgeR and/or p < 0.05
382 via t-test) (Figure 3E, F, Figure S6, Supplementary Table 5). Age-increasing sites linked
383 to *TMPRSS2* harbored sequence motifs for transcription factors such as NKX, FOXA,
384 CEBPA, and inflammation-related factors such as STAT, IRF, and FOS/JUN (Figure 3G)
385 many of which were corroborated by available ChIP-seq data in lung related samples (Oki
386 et al., 2018). Furthermore, at 12 of the 13 age-increasing sites, we uncovered additional

387 evidence for enhancer-related histone modifications from ENCODE supporting that they
388 have *cis*-regulatory activity (Figure 3H) (Consortium, 2012). When viewed in genomic
389 context these sites showed a clear age-dependent increase in read depth likely reflecting
390 a higher fraction of accessible nuclei (Figure 3I).

391
392 **Genetic variants predicted to affect age-increased *TMPRSS2* sites are associated**
393 **with respiratory phenotypes and *TMPRSS2* expression**

394 Mapping the discrete accessible chromatin sites at genes required for SARS-CoV-2
395 viral entry allowed us to next characterize non-coding sequence variation that might affect
396 regulation of these sites and contribute to phenotypic differences in the risk of lung
397 disease. In particular, we focused on the 37 sites linked to *TMPRSS2* activity including
398 13 with age-increased chromatin accessibility.

399 In total, 8,002 non-singleton sequence variants in the gnomAD v3 database
400 (Karczewski et al., 2019) overlapped a site either linked to or within 250kb of the
401 *TMPRSS2* promoter. To determine which of these variants might affect regulatory activity
402 in AT2 cells, we applied a machine learning approach (deltaSVM) (Lee et al., 2015) to
403 model AT2 chromatin accessibility and predict variants with allelic effects on chromatin
404 (see **Methods**). We identified 721 variants with significant effects (FDR<0.1) on AT2
405 chromatin accessibility, of which 148 mapped in an age-dependent site linked to
406 *TMPRSS2* (Figure 4A). Among these 148 variants, 14 were common (defined here as
407 minor allele frequency > 1%) in at least one major population group in gnomAD, several
408 of which were predicted to disrupt AT2 age-dynamic TF motifs such as FOS/JUN, IRF,
409 STAT, RUNX, NKX and ESR1 (Figure 4A). The common variants generally had
410 consistent frequencies across populations, except for rs35074065 which was much less
411 common in East Asians (EAS) relative to other populations (MAF=0.005, Figure 4B).

412 We next determined whether common variants with predicted AT2 regulatory effects
413 were associated with phenotypes related to respiratory function, infection, medication use
414 or other traits using GWAS data generated using the UK Biobank (UKBB) (Sudlow et al.,
415 2015). Across the 11 variants tested for association in UKBB data, the most significant
416 association was between rs35074065 and emphysema ($p=5.64 \times 10^{-7}$) (Figure 4C). This
417 variant was also more nominally associated ($p<0.005$) with asthma ($p=6.7 \times 10^{-4}$) and

418 influenza vaccine ($p=1.76\times 10^{-3}$). Furthermore, the majority of tested variants (8/11) were
419 nominally associated ($p<1\times 10^{-3}$) with at least one phenotype related to respiratory function
420 or respiratory medication use including salmeterol + fluticasone propionate, which is
421 commonly used to treat asthma and COPD (rs7279188 $p=1.3\times 10^{-5}$), bacterial pneumonia
422 (rs2838089 $p=2.4\times 10^{-4}$), bronchiectasis (rs9974995 $p=7.1\times 10^{-4}$, rs568517 $p=8.1\times 10^{-4}$),
423 and COPD (rs1557372 $p=2.9\times 10^{-3}$) (Figure 4C).

424 Given that common AT2 variants showed predicted regulatory function and
425 association with respiratory disease and infection phenotypes, we next asked whether
426 these variants regulated the expression of *TMPRSS2* using human lung eQTL data from
427 the GTEx v8 release. Among variants tested for association in GTEx, we observed a
428 highly significant eQTL for *TMPRSS2* expression at rs35074065 ($p=3.9\times 10^{-11}$) as well as
429 more nominal eQTL evidence at rs1557372 ($p=2.9\times 10^{-5}$) and rs9974995 ($p=3.5\times 10^{-6}$).
430 Furthermore, in fine-mapping data, rs35074065 had a high posterior probability
431 (PPA=41.6%) and therefore likely has a direct casual effect on *TMPRSS2* expression
432 (Figure 4D). This variant further disrupted sequence motifs for IRF and STAT transcription
433 factors, suggesting that its effects may be mediated through interferon signaling and anti-
434 viral programs (Figure 4D).

435 As the *TMPRSS2* eQTL at rs35074065 was identified in bulk lung samples, we finally
436 sought to determine the specific cell types driving the effects of this eQTL. Using cell type-
437 specific expression profiles derived from our snRNA-seq data, we estimated the
438 proportions of 14 different cell types present in the 515 bulk lung RNA-seq samples from
439 GTEx v8 (Figure 4E) (Aguet et al., 2019). We then tested the association between
440 rs35074065 and *TMPRSS2* expression while including estimated cell type proportions for
441 each sample in the eQTL model (see **Methods**). We observed highly significant
442 association when including AT2 cell proportion ($p=3.8\times 10^{-18}$) as well as macrophage
443 proportion ($p=4.0\times 10^{-12}$), supporting the possibility that the *TMPRSS2* eQTL at
444 rs35074065 acts through AT2 cells and macrophages (Figure 4F).

445

446

447 **DISCUSSION**

448 In this study, we focused on the lung, the organ at the center of COVID-19 morbidity
449 and mortality. We generated a snATAC-seq reference dataset of the healthy human lung
450 at three postnatal stages, and in parallel generated snRNA-seq data from the same
451 samples to allow comparison with gene expression. Importantly, datasets were produced
452 using uniform tissue procurement and single nucleus technologies for both modalities
453 across samples. This consistency allowed us to uncover age-associated dynamics in
454 gene expression and regulation. While we focus on COVID-19 related genes in this study,
455 the datasets more broadly enable in-depth analysis of cell-type resolved dynamics of
456 chromatin accessibility and gene expression in the human lung. We hope these datasets
457 will be further utilized by the community to enhance knowledge and treatment of lung
458 diseases.

459 One of the strongest findings that has been corroborated by multiple large-scale
460 epidemiological studies is that infants and children, while still susceptible to infection,
461 generally do not develop symptoms as severe as adults (Bi et al., 2020; CDC, 2020).
462 Although the underlying molecular basis of this skew is unclear and is likely multifactorial,
463 our data demonstrate that *ACE2*⁺ and *TMPRSS2*⁺ and *ACE2*⁺/*TMPRSS2*⁺ are detected
464 in a higher proportion of AT2 nuclei in adult samples compared to the younger samples.
465 These findings suggest that SARS-CoV-2 may enter proportionally fewer cells in younger
466 lungs compared to adult lungs, leading to tempered viral replication and damage. While
467 we await clinical validation of this finding, this difference in viral entry factors, in addition
468 to likely differences in immune response to viral infection, may explain the age-related
469 bias in COVID-19 severity.

470 The observed increase in the proportion of cells expressing viral entry genes is further
471 corroborated by age-related changes in accessible chromatin, which offers insight for
472 using gene regulatory mechanisms to restrict the expression of viral entry genes. For
473 example, at the *TMPRSS2* locus we identified 10 accessible chromatin sites that showed
474 significantly increased accessibility with age. These sites may therefore represent *cis*
475 regulatory elements that contribute to activation of *TMPRSS2* gene expression in an
476 increasing number of cells in adults and represent possible sites to modulate in order to
477 restrict expression. Furthermore, one of the age-dependent sites harbors a sequence

478 variant (rs35074065) significantly associated with *TMPRSS2* expression and respiratory
479 phenotypes, suggesting it may be of particular value in this context.

480 To explore potential avenues for manipulating the expression of viral entry genes, we
481 identified transcription factors enriched in sites with increased chromatin accessibility in
482 adult AT2 cells compared to younger AT2 cells. These included transcription factors
483 involved in stress and immune responses. For example, key interferon pathway-related
484 factors STAT and IRF have binding sites in the 10 age-increased *TMPRSS2* peaks. The
485 likely causal *TMPRSS2* eQTL variant rs35074065 is predicted to disrupt STAT and IRF
486 binding, raising the possibility that STAT and/or IRF binding at this site may directly control
487 *TMPRSS2* gene expression.

488 While our findings suggest that interferon pathway transcription factors may play a
489 role in regulating the expression of SARS-CoV-2 entry genes such as *TMPRSS2*,
490 extensive preclinical studies are needed to validate this regulation in an *in vivo* context.
491 As a key anti-viral factor, interferon is stimulated in host cells upon infection by viruses,
492 likely including SARS-CoV-2 (Lukhele et al., 2019; Mesev et al., 2019; Xia et al., 2018).
493 The literature contains conflicting data regarding whether and how viral infection may act
494 through the interferon pathway to regulate viral entry gene expression. For example,
495 binding of the original SARS-CoV spike protein to ACE2 receptor in mice led to reduced
496 *Ace2* expression in the lung (Kuba et al., 2005). However, a recent single-cell study
497 suggested that viral-induced interferon activation stimulates *ACE2* expression (Ziegler,
498 2020). We caution that the potential effect of interferon signaling on COVID-19 needs to
499 be investigated beyond viral entry, as the pathway likely has distinct roles in the different
500 phases of the disease.

501 In our lung snRNA-seq data, *ACE2* is detected in a very small number of cells, a
502 finding that is corroborated by a number of recent single cell studies (Qi et al., 2020;
503 Waradon Sungnak, 2020; Zhao et al., 2020; Ziegler, 2020; Zou et al., 2020). The low
504 fraction of nuclei that are *ACE2* positive could be due to low overall expression which in
505 turn results in significant dropout in single cell or single nucleus RNA-seq. This suggests
506 the possibility that *ACE2* may not be needed at high levels for viral attachment to host
507 cells. Alternatively, it is plausible that alternative receptors such as BSG also facilitate
508 SARS-CoV-2 attachment *in vivo*. Compared to *ACE2*, *BSG* is expressed and co-

509 expressed with proteases in a higher fraction of nuclei in AT2 and in additional cell types
510 in the human lung.

511 To limit SARS-CoV-2 infection by manipulating the expression of viral entry proteins,
512 we caution that inhibiting *ACE2* expression should not be a recommended strategy. Aside
513 from being a viral receptor gene, *ACE2* is also required for protecting the lung from injury-
514 induced acute respiratory distress phenotypes, the precise cause of COVID-19 mortality
515 (Imai et al., 2005). Thus, inhibiting *ACE2* expression may compromise the ability of the
516 lung to sustain damage. In comparison, *Tmprss2* mutant mice show no defects at
517 baseline and are more resistant to the original SARS-CoV infection (Iwata-Yoshikawa et
518 al., 2019; Kim et al., 2006). Thus, manipulating the expression of genes such as
519 *TMPRSS2* may represent a safer path to limit SARS-CoV-2 viral entry. *TMPRSS2* is also
520 involved in the entry of other respiratory viruses such as influenza, suggesting that
521 modulating its expression may also be effective in deterring entry and spread of other
522 viruses (Limburg et al., 2019).

523 In this study, we present the first snATAC-seq dataset of the human lung and
524 complementary snRNA-seq data from the same samples. Here, we used COVID-19
525 genes to demonstrate how this dataset can be utilized. As COVID-19 GWAS data
526 emerge, our datasets will offer a powerful cell type-resolved platform to interrogate
527 mechanisms that may underlie genetic differences in the susceptibility and response to
528 SARS-CoV-2 infection. Furthermore, our results suggest that modulation of the interferon
529 pathway is a possible avenue to restrict *TMPRSS2* expression and viral entry.
530 Identification of regulators that restrict the expression of viral entry genes without
531 detrimentally affecting other aspects of the normal antiviral response will be a safe and
532 effective strategy towards combating COVID-19. We note that this work is a product of
533 the NHLBI-funded LungMap consortium, and our joint goal is to provide the community
534 with fundamental knowledge of the human lung to help combat COVID-19.

535

536

537 **ACKNOWLEDGEMENTS**

538 We are extremely grateful to the families who have generously given such precious
539 gifts to support this research. We thank all the members of the LungMAP Consortium for
540 their collaborations. We thank Dr. Bing Ren, Dr. Maike Sander, members of the Sun lab,
541 Gaulton lab, Ren lab and the UCSD Center for Epigenomics for insightful discussions.
542 We thank S. Kuan for sequencing and B. Li for bioinformatics support. We thank K.
543 Jepsen and the UCSD IGM Genomics Center for sequencing the snRNAseq libraries. We
544 thank the QB3 Macrolab at UC Berkeley for purification of the Tn5 transposase.

545 Funding: This work was supported by NHLBI Molecular Atlas of Lung Development
546 Program Research Center grant 1U01 HL148867 (to X.Sun, S. Preissl, A. Wang and J.
547 Verheyden), and Human Tissue Core grant U01HL122700 / HL148861 (to G.H. Deutsch,
548 T.J. Mariani, G.S. Pryhuber). Work at the Center for Epigenomics was supported in part
549 by the UC San Diego School of Medicine.

550

551

552 **AUTHOR CONTRIBUTIONS**

553 Conceptualization: A.W., K.J.G., S.P., X.S.; Methodology: A.W., K.J.G., S.P., K.Z.;
554 Validation: J.M.V., R.E.Y., J.B.; Formal analysis: A.W., K.J.G., S.P., J.C., O.B.P., J.B.,
555 M.J.V., J.M.N., M.G., Y.X.; Investigation: J.B., J.M.V., X.H.; Resources: R.M., H.H., L.R.,
556 C.P., G.P., J.A.W.; Data curation: A.W., K.J.G., S.P., J.C., O.B.P., J.B., M.J.V., P.K.,
557 D.A.F; Writing: A.W., J.C., J.M.V., K.J.G., S.P., X.S.; Supervision: A.W., K.J.G., S.P.,
558 J.A.W., X.S.; Project administration: A.W., K.J.G., S.P., J.M.V., X.S.; Funding acquisition:
559 A.W., K.J.G., S.P., J.M.V., X.S.

560

561 **FIGURE LEGENDS**

562

563 **Figure 1. snRNA-seq of human lungs reveals expression of SARS-CoV-2 cell entry**
564 **genes in the epithelial cell lineage. A** UMAP embedding and clustering result of 46,500
565 snRNA-seq data from 9 donors (Premature born (30 week^{GA} of pregnancy), 3 yo, 30 yo;
566 n = 3 per time point) identifies 31 clusters. Each dot represents a nucleus. Spread-out
567 grey dots correspond to nuclei of unclassified cluster. **B, C** Cluster specific violin blots of
568 gene expression of **B** *ACE2* and **C** *TMPRSS2*. **D, E** Fraction of AT2 cells with expression
569 of *ACE2* and *TMPRSS2* at each time point. All data are represented as mean \pm SD. p
570 values derived from t-tests; One-way ANOVA did not reach significance. **F** Box plot of log
571 normalized expression of *TMPRSS2* in AT2 cells at each time point. Displayed are the
572 median expression values for AT2 nuclei in individual samples with at least 1 UMI.

573

574 **Figure 2. snATAC-seq analysis of human lungs reveals candidate cis regulatory**
575 **elements for *ACE2* and *TMPRSS2*. A** UMAP embedding and clustering results of
576 snATAC-seq data from 90,980 single-nucleus chromatin profiles from ten donors
577 (Premature born (30 week^{GA}, n = 3), 4 month old (n = 1), 3 yo (n = 3) and 30 yo (n = 3)).
578 **B** Gene accessibility of candidate SARS-CoV-2 cell entry genes. **C** Union set of peaks
579 identified in all clusters surrounding *ACE2* (+/- 650 kb) and elements that show co-
580 accessibility (co-accessibility score > 0.05) with the *ACE2* promoter via Cicero
581 (Cusanovich et al., 2018) (top panel). Hierarchical clustering of the relative proportion of
582 cells (see methods) with a fragment within 165 peak regions surrounding *ACE2* (lower
583 panel). Asterisks highlight peaks co-accessible with the *ACE2* promoter via Cicero.
584 Horizontal red box highlights peaks with increased relative accessibility shared in basal,
585 ciliated, AT1, AT2 and club cells as compared to other cell types. Vertical red box
586 highlights peaks with increased relative accessibility in AT2 cells. **D** Union set of peaks
587 identified in all clusters surrounding *TMPRSS2* (+/- 650 kb) and elements that show co-
588 accessibility with the *TMPRSS2* promoter (top panel; co-accessibility score >0.05
589 (Cusanovich et al., 2018)). Hierarchical clustering of the relative proportion of cells with a
590 fragment within 289 peak regions surrounding *TMPRSS2* (lower panel). Horizontal red
591 box highlights peaks with increased relative accessible cells shared in basal, ciliated,

592 club, AT1 and AT2 cells as compared to other cell types. Vertical red box highlights peaks
593 with increased relative accessibility in AT2 cells. Asterisks highlight peaks co-accessible
594 with the *TMPRSS2* promoter.

595

596 **Figure 3. Age-increasing accessible chromatin in AT2 cells exhibits signatures of**
597 **immune regulation and harbors *TMPRSS2*-linked sites of chromatin accessibility.**

598 **A** Differential analysis was performed on AT2 cells using pairwise comparisons between
599 three ages with replicates (n = 3 per stage). **B** K-means cluster analysis (K=5) of relative
600 accessibility scores (see **Methods**) for 22,845 age-dynamic peaks (FDR < 0.05, EdgeR)
601 in AT2 cells. Clusters III and IV show increasing accessibility with age and contain seven
602 *TMPRSS2*-co-accessible sites. **C** GREAT (McLean et al., 2010) analysis of elements in
603 group cIII (left panel) and cIV (right panel) shows enrichment of immune related gene
604 ontology terms. **D** Transcription factor motif enrichment analysis of elements in cIII and
605 cIV. **E** Classification of age-dynamic patterns across the 37 *TMPRSS2*-co-accessible sites
606 based on the relative percentage of AT2 cells with at least one fragment overlapping each
607 peak. Red bars indicate dynamic peaks identified from analysis in B (FDR < 0.05, EdgeR).
608 **F** Locus restricted differential analysis of *TMPRSS2*-linked peaks with increased
609 accessibility in AT2 with aging (top panel in 3E). Black asterisk, p < 0.05 (T-test); Red
610 asterisk, FDR < 0.05 (EdgeR) from dynamic peak analysis in B. **G** Annotation of motifs
611 and evidence for transcription factor association within age-increased peaks. Blue bar,
612 Motif present (FIMO); Green bar, Motif present (FIMO) and transcription factor
613 association (ChIP-Atlas). **H** Overlap with ENCODE histone modification ChIP-seq data
614 (Consortium, 2012) from SCREEN. **I** Genome browser representation of four *TMPRSS2*-
615 linked peaks across age groups.

616
617 **Figure 4. Genetic variants predicted to affect age-increasing AT2 accessible**
618 **chromatin are associated with respiratory phenotypes and *TMPRSS2* expression.**

619 **A** Top: genome browser view of sites linked to *TMPRSS2* activity including those with
620 age-dependent increase in activity. Right: Non-singleton genetic variants in gnomAD v3
621 mapping in each age-dependent site with predicted effects (FDR<.10) on AT2 chromatin
622 accessibility using deltaSVM. Variants within each site are organized based on whether

623 the reference (ref) or alternate (alt) allele has a higher predicted effect. Left: DeltaSVM
624 scores of variants with predicted effects on AT2 chromatin accessibility and common
625 (defined as MAF>1%) in at least one major population group in gnomAD v3, annotated
626 with sequence motifs overlapping the variant for TF families enriched in age-increased
627 AT2 sites. **B** Population frequency of variant rs35074065, which had predicted AT2
628 effects and was present at much lower frequency in East Asians relative to other
629 population groups. AFR: African, AMR: Latino/American, ASJ: Ashkenazi Jewish, EAS:
630 East Asian, FIN: Finnish, EUR: European (non-Finnish). **C** Association of common
631 variants with predicted AT2 effects with human phenotypes in the UK Biobank. The
632 majority of tested variants show at least nominal evidence ($p < 0.005$) for association with
633 phenotypes related to respiratory disease, infection and medication. **D** Fine-mapping
634 probabilities for an *TMPRSS2* expression QTL in human lung samples from the GTEx
635 project release v8. The variant rs35074065 has the highest casual probability (PPA=.42)
636 for the eQTL, maps in an age-dynamic AT2 site and is predicted to disrupt binding of IRF
637 and STAT TFs. Variants are colored based on r^2 with rs35074065 in 1000 Genomes
638 Project data using all populations. **E** Estimated cell type proportions for 515 human lung
639 samples from GTEx derived using cell type-specific expression profiles for cell types with
640 more than 500 cells from snRNA-seq data generated in this study. **F** Association p-values
641 between rs35074065 genotype and *TMPRSS2* lung expression after including an
642 interaction term between genotype and estimated cell type proportions for each sample.
643 We observed stronger eQTL association when including an interaction with AT2 cell
644 proportion as well as macrophage proportion.

645 **METHODS**

646

647 **Human subjects and tissue collection**

648 Donor lung samples were provided through the federal United Network of Organ
649 Sharing via National Disease Research Interchange (NDRI) and International Institute for
650 Advancement of Medicine (IIAM) and entered into the NHLBI LungMAP Biorepository for
651 Investigations of Diseases of the Lung (BRINDL) at the University of Rochester Medical
652 Center overseen by the IRB as RSRB00047606, as previously described (Ardini-Poleske
653 et al., 2017; Bandyopadhyay et al., 2018). Portions (0.25-1.0 cm³) of small airway region
654 of right middle lobe (RML) lung tissue were frozen in cryovials over liquid nitrogen and
655 placed at -80°C for storage. Upon request, while kept frozen on dry ice, a tissue piece
656 (approximately 100 mg) was chipped off the sample. These smaller samples were then
657 shipped in cryovials to UCSD on an abundance of dry ice.

658

659 **Single nucleus ATAC-seq data generation**

660 Combinatorial barcoding single nucleus ATAC-seq was performed as described
661 previously with modifications (Cusanovich et al., 2015; Fang et al., 2019; Preissl et al.,
662 2018) and using new sets of oligos for tagmentation and PCR (Supplementary Table 8).
663 Briefly, for each sample, lung tissue was homogenized using mortar and pestle on liquid
664 nitrogen. 1 ml nuclei permeabilization buffer (10mM Tris-HCL (pH 7.5), 10mM NaCl, 3mM
665 MgCl₂, 0.1% Tween-20 (Sigma), 0.1% IGEPAL-CA630 (Sigma) and 0.01% Digitonin
666 (Promega) in water (Corces et al., 2017)) was added to 30 mg of ground lung tissue and
667 tissue was resuspended by pipetting for 8-15 times. Nuclei suspension was incubated for
668 10 min at 4°C and filtered with 30 µm filter (CellTrics). Nuclei were pelleted with a swinging
669 bucket centrifuge (500 x g, 5 min, 4°C; 5920R, Eppendorf) and resuspended in 500 µL
670 high salt tagmentation buffer (36.3 mM Tris-acetate (pH = 7.8), 72.6 mM potassium-
671 acetate, 11 mM Mg-acetate, 17.6% DMF) and counted using a hemocytometer.
672 Concentration was adjusted to 2,000 nuclei/9 µl, and 2,000 nuclei were dispensed into
673 each well of one 96-well plate. For tagmentation, 1 µL barcoded Tn5 transposomes (Fang
674 et al., 2019) was added using a BenchSmart™ 96 (Mettler Toledo), mixed five times and
675 incubated for 60 min at 37 °C with shaking (500 rpm). To inhibit the Tn5 reaction, 10 µL

676 of 40 mM EDTA were added to each well with a BenchSmart™ 96 (Mettler Toledo) and
677 the plate was incubated at 37 °C for 15 min with shaking (500 rpm). Next, 20 µL 2 x sort
678 buffer (2 % BSA, 2 mM EDTA in PBS) was added using a BenchSmart™ 96 (Mettler
679 Toledo). All wells were combined into a FACS tube and stained with 3 µM Draq7 (Cell
680 Signaling). Using a SH800 (Sony), 20 2n nuclei were sorted per well into eight 96-well
681 plates (total of 768 wells) containing 10.5 µL EB (25 pmol primer i7, 25 pmol primer i5,
682 200 ng BSA (Sigma). Preparation of sort plates and all downstream pipetting steps were
683 performed on a Biomek i7 Automated Workstation (Beckman Coulter). After addition of 1
684 µL 0.2% SDS, samples were incubated at 55 °C for 7 min with shaking (500 rpm). 1 µL
685 12.5% Triton-X was added to each well to quench the SDS. Next, 12.5 µL NEBNext High-
686 Fidelity 2× PCR Master Mix (NEB) were added and samples were PCR-amplified (72 °C
687 5 min, 98 °C 30 s, (98 °C 10 s, 63 °C 30 s, 72°C 60 s) × 12 cycles, held at 12 °C). After
688 PCR, all wells were combined. Libraries were purified according to the MinElute PCR
689 Purification Kit manual (Qiagen) using a vacuum manifold (QIAvac 24 plus, Qiagen) and
690 size selection was performed with SPRI Beads (Beckmann Coulter, 0.55x and 1.5x).
691 Libraries were purified one more time with SPRI Beads (Beckmann Coulter, 1.5x).
692 Libraries were quantified using a Qubit fluorimeter (Life technologies) and the
693 nucleosomal pattern was verified using a TapeStation (High Sensitivity D1000, Agilent).
694 The library was sequenced on a HiSeq4000 or NextSeq500 sequencer (Illumina) using
695 custom sequencing primers with following read lengths: 50 + 10 + 12 + 50 (Read1 +
696 Index1 + Index2 + Read2). Primer and index sequences are listed in Supplementary
697 Table 8.

698

699 **Single nucleus RNA-seq data generation**

700 Droplet-based Chromium Single Cell 3' solution (10x Genomics, v3 chemistry)(Zheng
701 et al., 2017) was used to generate snRNA-seq libraries. Briefly, 30 mg pulverized lung
702 tissue was resuspended in 500 µl of nuclei permeabilization buffer (0.1% Triton X-100
703 (Sigma-Aldrich, T8787), 1X protease inhibitor, 1 mM DTT, and 0.2 U/µl RNase inhibitor
704 (Promega, N211B), 2% BSA (Sigma-Aldrich, SRE0036) in PBS). Sample was incubated
705 on a rotator for 5 minutes at 4°C and then centrifuged at 500 rcf for 5 minutes (4°C, run
706 speed 3/3). Supernatant was removed and pellet was resuspended in 400 µl of sort buffer

707 (1 mM EDTA 0.2 U/μl RNase inhibitor (Promega, N211B), 2% BSA (Sigma-Aldrich,
708 SRE0036) in PBS) and stained with DRAQ7 (1:100; Cell Signaling, 7406). 75,000 nuclei
709 were sorted using a SH800 sorter (Sony) into 50 μl of collection buffer consisting of 1 U/μl
710 RNase inhibitor in 5% BSA; the FACS gating strategy sorted based on particle size and
711 DRAQ7 fluorescence. Sorted nuclei were then centrifuged at 1000 rcf for 15 minutes (4°C,
712 run speed 3/3) and supernatant was removed. Nuclei were resuspended in 35 μl of
713 reaction buffer (0.2 U/μl RNase inhibitor (Promega, N211B), 2% BSA (Sigma-Aldrich,
714 SRE0036) in PBS) and counted on a hemocytometer. 12,000 nuclei were loaded onto a
715 Chromium controller (10x Genomics). Libraries were generated using the Chromium
716 Single Cell 3' Library Construction Kit v3 (10x Genomics, 1000078) according to
717 manufacturer specifications. CDNA was amplified for 12 PCR cycles. SPRISelect reagent
718 (Beckman Coulter) was used for size selection and clean-up steps. Final library
719 concentration was assessed by Qubit dsDNA HS Assay Kit (Thermo-Fischer Scientific)
720 and fragment size was checked using TapeStation High Sensitivity D1000 (Agilent) to
721 ensure that fragment sizes were distributed normally about 500 bp. Libraries were
722 sequenced using the NextSeq500 and a HiSeq4000 (Illumina) with these read lengths:
723 28 + 8 + 91 (Read1 + Index1 + Read2).

724

725 **Single nucleus RNA-seq analysis**

726 Sequencing reads were demultiplexed (cellranger mkfastq) and processed (cellranger
727 count) using the Cell Ranger software package v3.0.2 (10x Genomics). Reads were
728 aligned to the human reference hg38 (Cell Ranger software package v3.0.2). Reads
729 mapping to intronic and exon sequences were retained. Resulting UMI feature-barcode
730 count matrices were loaded into Seurat (Stuart et al., 2019). All genes represented in ≥ 3
731 nuclei and cells with 500-4000 detected genes were included for downstream processing.
732 UMI counts were log-normalized and scaled by a factor of 10,000 using the
733 NormalizeData function. Top 3000 variable features were identified using the
734 FindVariableFeatures function and finally scaled using the ScaleData function. Barcode
735 collisions were removed for individual datasets using DoubletFinder (McGinnis et al.,
736 2019) with following parameters: pN = 0.15 and pK = 0.005, anticipated collision rate =
737 10%. Clusters were assigned a doublet score (pANN) and classification as “doublet” or

738 “singlet”; called doublets and cells with a pANN score > 0 were removed. UMI matrices
739 for datasets were merged and corrected for batch effects due to experiment date, donor,
740 and sex using the Harmony package (Korsunsky et al., 2019). UMAP coordinates and
741 clustering were performed using the RunUMAP, FindNeighbors, and FindClusters
742 functions in Seurat with principal components 1-23, 25-26, and 28. Clusters were
743 annotated, and putative doublets as defined by expression of canonically mutually
744 exclusive markers were excluded from analysis; remaining cells were re-clustered using
745 the previously described parameters. Final cluster annotation was done using canonical
746 markers. For genes of interest such as (e.g. *ACE2*, *TMPRSS2*), nuclei with at least one
747 UMI for the gene were considered “expressing”. To analyze changes in percentage of
748 nuclei expressing we performed One-way ANOVA (ANalysis Of VAriance) with post-hoc
749 Tukey HSD (Honestly Significant Difference) using GraphPad Prism version 8.0.0 for
750 Windows, GraphPad Software, San Diego, California USA, www.graphpad.com. Due to
751 one potential outlier in the 30wkGA group (D062) we performed in addition a simple t-test
752 comparing 3 yr to 30 yr groups. Differential gene expression analysis between *ACE2*⁺
753 and *ACE2*⁻ AT2 cells we used FindAllMarkers with parameters logfc = 0, min.pct = 0,
754 test.use = “wilcox”, verbose = TRUE.

755 756 **Normalization and comparison of gene expression frequency across snRNA-seq** 757 **and scRNA-seq datasets**

758 Single cell RNA-seq (10x Genomics 3’ v2) of 4 aged (>55yr) control lungs were
759 obtained from publicly available data (Morse et al., 2019; Reyfman et al., 2019). Raw
760 gene expression matrices were downloaded from Gene Expression Omnibus (GEO)
761 repository (GSE128033 and GSE122960). Cells were filtered using the following
762 commonly used criteria: >500 expressed genes and <10% UMIs mapped to mitochondrial
763 DNAs. In addition, cells with greater than or equal to 40,000 UMIs were excluded from
764 the downstream analysis; this filtration criterion was selected based on the distribution of
765 UMIs in single cells in individual donors. Seurat (version 3) (Stuart et al., 2019) was used
766 to identify AT2 cells from individual aged donors. Nuclei from the 9 libraries generated in
767 this study and cells from libraries for the 4 aged donors were integrated using the Seurat
768 3 standard integration pipeline (Stuart et al., 2019).

769 We calculated *ACE2* and *TMPRSS2* expression frequency in AT2 cells (percentage
770 of AT2 cells with >0 UMI) in individual donors. We then performed median based
771 normalization, so all donors reached the same median value. In calculating the median
772 value for each donor, the expression frequency values of genes (n=26,260) common in
773 both datasets were used.

774

775 **Single nucleus ATAC-seq analysis**

776 For each sequenced snATAC-Seq libraries, we obtained four FASTQ files paired-end
777 DNA reads as well as the combinatorial indexes for i5 (768 different PCR indices) and T7
778 (96 different tagmentation indices; Supplementary Table 8). We selected all reads with
779 ≤ 2 mistakes per individual index (Hamming distance between each pair of indices is 4)
780 and subsequently integrated the full barcode at the beginning of the read name in the
781 FASTQ files (<https://gitlab.com/Groumf/ATACdemultiplex/>). Next, we used trim galore
782 (v.0.4.4) to remove adapter sequences from reads prior to read alignment. We aligned
783 reads to the hg19 reference genome using bwa mem (v.0.7.17) (Li and Durbin, 2009) and
784 subsequently used samtools (Li et al., 2009) to remove unmapped, low map quality
785 (MAPQ<30), secondary, and mitochondrial reads. We then removed duplicate reads on
786 a per-cell basis using MarkDuplicates (BARCODE_TAG) from the picard toolkit. As an
787 initial quality cutoff, we set a minimum of 1,000 reads (unique, non-mitochondrial) and
788 observed 120,090 cells passing this threshold.

789 We used a previously described pipeline to identify snATAC-seq clusters (Chiou et
790 al., 2019). Briefly, we used scanpy (Wolf et al., 2018) to uniform read depth-normalize
791 and log-transform read counts within 5 kb windows. We then identified highly variable (*hv*)
792 windows (min_mean=0.01, min_disp=0.25) and regressed out the total read depth across
793 *hv* windows (usable counts) within each experiment. We then merged cells across
794 experiments and extracted the top 50 PCs, using Harmony (Korsunsky et al., 2019) to
795 correct for potential confounding factors including donor-of-origin and biological sex. We
796 used Harmony-corrected components to build a nearest neighbor graph
797 (n_neighbors=30) using the cosine metric, which was used for UMAP visualization
798 (min_dist=0.3) and Leiden clustering (resolution=1.5) (Traag et al., 2019).

799 Prior to the final clustering results, we performed iterative clustering to identify and
800 remove cells mapping to clusters with aberrant quality metrics. First, we removed 3,183
801 cells mapping in clusters with low read depth. Next, we removed 20,718 cells mapping in
802 clusters with low fraction of reads in peaks. Finally, we re-clustered the cells at high
803 resolution and removed 5,209 cells mapping in potential doublet sub-clusters. On
804 average, these sub-clusters had higher usable counts, promoter usage, and accessibility
805 at more than one marker gene promoter. After removing all of these cells, our final clusters
806 consisted of 90,980 cells. To identify marker genes for each cluster, we used linear
807 regression models with gene accessibility as a function of cluster assignment and usable
808 counts across single cells.

809

810 **Computing relative accessibility scores**

811 We define an accessible locus as the minimal genomic region that can be bound and
812 cut by the enzyme. We use $L \subset N$ to represent the set of all accessible loci. We further
813 define a pseudo-locus as the set of accessible loci that relates to each other in a certain
814 meaningful way (for example, nearby loci, loci from different alleles). In this example,
815 pseudo-loci correspond to peaks. We use $\{d_i \mid d_i \subset L\}$ to represent the set of all pseudo-
816 loci. Let a_l be the accessibility of accessible locus l , where $l \in L$. We define the
817 accessibility of pseudo-locus d_i as $A_i = \sum_{k \in d_i} a_k$, i.e., the sum of accessibility of
818 accessible loci associated with d_i . Let C_j be the library complexity (the number of distinct
819 molecules in the library) of cell j . Assuming unbiased PCR amplification, then the
820 probability of being sequenced for any fragment in the library is: $s_j = 1 - (1 - \frac{1}{C_j})^{k_j}$, where
821 k_j is the total number of reads for cell j . If we assume that the probability of a fragment
822 present in the library is proportional to its accessibility and the complexity of the library,
823 then we can deduce that the probability of a given locus l in cell j being sequenced is:
824 $p_{lj} \propto a_l C_j s_j$. For any pseudo-locus d_i , the number of reads in d_i for cell j follows the
825 Poisson binomial distribution, and its mean is $m_{ij} = \sum_{k \in d_i} p_{kj} \propto C_j s_j \sum_{k \in d_i} a_k = C_j s_j A_i$.
826 Given a pseudo-locus (or peak) by cell count matrix O , we have: $\sum_j O_{ij} = \sum_j m_{ij}$.
827 Therefore, $A_i = Z \frac{\sum_j O_{ij}}{\sum_j C_j s_j}$, where Z is a normalization constant. When comparing across

828 different samples the relative accessibility may be desirable as they sum up to a constant,
829 *i.e.*, $\sum_i A_i = 1 \times 10^6$. In this case, we can derive $A_i = \frac{\sum_j o_{ij}}{\sum_{ij} o_{ij}} * 10^6$.

830

831 **Calculating the relative percent of cells with accessibility at a locus**

832 To correct for biases occurring from differential read depths between clusters, we used
833 the following strategy to determine the relative ratio of cells with accessibility at a given
834 locus. We defined the set of accessible loci L of a given dataset D as the genomic regions
835 covered by the set peaks P inferred from D . We define X the set of cells from D , and S a
836 partitioning of X . For a given partition $S_i \in S$ and for each feature $p_j \in P$, we computed
837 m_{ij} the ratio of cells from S_i with at least one read overlapping p_j . We then defined the
838 score s_{ij} of loci p_j in S_i as $s_{ij} = 10^6 \cdot \frac{m_{ij}}{\sum_{j \in P} m_{ij}}$. We finally define the relative ratio of cells
839 normalized across the different clusters as $RS_{ij} = \frac{s_{ij}}{\sum_{i \in S} s_{ij}}$.

840

841 **Associating promoters to candidate distal regulatory elements.**

842 To identify AT2 co-accessible loci with the promoters of *TMPRSS2*, *ACE2*, *FURIN*,
843 *BSG*, and *CTSL* we used Cicero (Pliner et al., 2018). First, we performed a Cicero
844 analysis for each individual cluster using a genomic window of 1 Mb (co-accessibility
845 score >0.05). In addition, we performed Cicero using a random subset of 15,000 nuclei
846 from the complete dataset and a genomic window of 250 kb (co-accessibility score >0.05).
847 We then defined the promoter regions of *ACE2*, *TMPRSS2*, *FURIN*, *BSG*, and *CTSL* as
848 transcriptional start site (TSS) +/- 1 kb and selected the sites co-accessible with each of
849 the promoters (co-accessibility score >0.05). Finally, we merged the elements co-
850 accessible with the gene promoters from both analyses to generate a union set of
851 candidate elements.

852

853 **Identification and clustering of AT2 peaks with changes in chromatin accessibility** 854 **genome-wide**

855 We used edgeR (Robinson et al., 2010) to identify differential accessible peaks
856 between each of pair of time points. As input we used the 122,352 peaks in AT2 cell.

857 Dataset ID and sex were used as technical covariates. Sites with False Discovery Rate
858 (FDR) < 0.05 after Benjamini-Hochberg correction were considered significant. Next, we
859 performed K-means using the relative accessibility score with a *loci x timepoints* matrix.
860 We used K from 5 to 8 and computed the Davis-Bouldin index to determine the best K to
861 partition the loci. let $R_{xy} = \frac{(s_x + s_y)}{d_{xy}}$ with s_x the average distance of each sample from cluster
862 x and d_{xy} the distance between the centroids of clusters x and y . The Davies-Bouldin
863 index is defined as $DB = \frac{1}{K} \sum_{x,y \in \text{clusters}} \max_{x \neq y} (R_{xy})$ and low DB scores indicate better partitioning.
864 We obtained an optimal partition with K=5.

865
866 **Identification of AT2 peaks with changes in chromatin accessibility at candidate**
867 **gene loci**

868 The ensemble of cells X from D can be divided per timepoint, cell subtype, or donor.
869 We identified for individual donors the relative % of cells with at least one read in peaks
870 associated with *ACE2*, *TMPRSS2*, *FURIN*, *BSG*, and *CTSL* promoters. As a background
871 to calculate the relative % of cells, we used the merged set of peaks from all the clusters.
872 Then, we computed a Student test for two independent samples with equal variance for
873 each pair of categories: 30 wk^{GA}, 3 yo and 30 yo. For each element the relative % of cells
874 were used as measurement variable and the timepoint as nominal variable.

875
876 **Annotation of genomic elements**

877 The GREAT algorithm (McLean et al., 2010) was used to annotate distal genomic
878 elements using the following settings: 2 nearest gene within 1Mb.

879
880 **Transcription factor related analyses**

881 *De novo* motif enrichment analysis in genomic elements was performed using
882 HOMER (Heinz et al., 2010) with standard parameters. Motif scanning was performed
883 using FIMO (Grant et al., 2011) online interface and default parameters. Motif files were
884 downloaded from JASPAR (Fornes et al., 2020) in MEME format. Motifs scanned were
885 MA0102.4 (CEBPA), MA0673.1(NKX2-8), MA0153.1(HNF1B), MA0503.1(NKX2-5),
886 MA0877.2(BARHL1), PB0022.1(GATA5), MA0490.1(JUNB), PH0171.1(NKX2-1),

887 MA0148.1(FOXA1), MA0144.1(STAT3), MA0517.1(STAT1::STAT2), MA0050.1(IRF),
888 MA0007.2(AR), and MA0592.1(ESRRA). To identify overlap with TF ChIP-seq sites, we
889 used ChIP-atlas (Oki et al., 2018). We downloaded a BED file for “TFs and other” antigens
890 across all lung related samples from the Peak Browser. We intersected these peaks with
891 the *TMPRSS2*-linked peaks and the FIMO motifs (Grant et al., 2011). In addition, we
892 downloaded enhancer related histone modifications (H3K4me1, H3K27ac) from the
893 SCREEN database and intersected with the peak lists (Consortium, 2012).

894

895 **Predicting variant effects on chromatin accessibility**

896 We used deltaSVM (Lee et al., 2015) to predict the effects of variants on chromatin
897 accessibility in AT2 cells. First, we extracted the sequences underlying AT2 sites that
898 were promoter-distal ($>\pm 500$ bp from GENCODE v19 transcript TSS for protein-coding
899 and long non-coding RNA genes). As described previously (Chiou et al., 2019), we trained
900 an AT2 sequence-based model and used it to predict effects for all possible combinations
901 of 11mers. Next, to compile a comprehensive set of variants to test, we downloaded lists
902 of variants from gnomAD v3 (Karczewski et al., 2019) and filtered out variants that were
903 singletons or indels longer than 3 bp. We then used the liftOver (Tyner et al., 2017) utility
904 to transform GRCh38 into GRCh37/hg19 coordinates. We retained variants from either
905 dataset that mapped within *TMPRSS2* linked sites and extracted sequences in a 19 bp
906 window around each variant (± 9 bp flanking each side). Finally, we calculated deltaSVM
907 z-scores for each variant by predicting deltaSVM scores, randomly permuting 11mer
908 effects and re-predicting deltaSVM scores, and using the parameters of the null
909 distribution to calculate deltaSVM z-scores. From the z-scores, we calculated p-values
910 and q-values and defined variants with significant effects using a threshold of $FDR < 0.1$.
911 We identified common variants defined as minor allele frequency $> .01$ in at least one
912 major population group. For each common variant, we obtained sequence surrounding
913 each variant allele and predicted sequence motifs from the JASPAR database (Fornes et
914 al., 2020) using FIMO (Grant et al., 2011), and focused on motifs of TF families enriched
915 in age-dependent AT2 chromatin.

916

917 **Phenotype associations for predicted effect variants**

918 We downloaded UK biobank round 2 GWAS combined sex results (Lab, 2020; Sudlow
919 et al., 2015). We used broad disease categories from the ICD-10-CM to classify ICD10
920 phenotypes, except for ICD10 codes relating to unclassified symptoms, external causes
921 of morbidity, and factors influencing health status and contact with health services. We
922 combined all non-cancer, self-reported diseases into a single category (self-reported) as
923 well as all treatments and medications (medication). We then extracted GWAS
924 association results for variants that were not tagged as low confidence variants, had
925 significant deltaSVM effects, and mapped in *TMPRSS2*-linked aging-related sites. From
926 these variants, we removed one (rs199938061) which was in perfect linkage
927 disequilibrium with another variant.

928

929 **Deconvoluting the *TMPRSS2* lung eQTL**

930 We used MuSiC (v.0.1.1) (Wang et al., 2019) to estimate the proportions of lung cell
931 types with >500 cells from our scRNA-seq dataset in lung bulk RNA-seq samples from
932 the GTEx v8 release (Aguet et al., 2019). We combined cell type labels for capillary (distal
933 and proximal), macrophages (M1 and M2), matrix fibroblasts (1 and 2), and NK/T cells.
934 We modeled the relationship between TMM-normalized *TMPRSS2* expression as a
935 function of the interaction between genotype and cell type proportion, while considering
936 the covariates used in the original GTEx data including sex, sequencing platform, PCR,
937 5 genotype PCs, and 59 inferred PCs from the expression data. From the original inferred
938 PCs, we excluded inferred PC 1 because it was highly correlated with AT2 cell type
939 proportion (Spearman $\rho=0.67$).

940

941 **SUPPLEMENTARY FIGURE LEGENDS**

942

943 **Figure S1. Quality control of snRNA-seq and snATAC-seq datasets. A**

944 Representative UMI barcode distribution output from CellRanger pipeline for snRNA-seq
945 libraries from human lung. **B** Number of nuclei passing quality control filtering for snRNA-
946 seq libraries. **C** Genes detected per nucleus. **D** Sequencing saturation of snRNA-seq
947 libraries. **E** Nuclei with less than 1,000 uniquely mapped reads were filtered from
948 snATAC-seq datasets. **F** Number of nuclei passing quality control filtering for snATAC-
949 seq libraries. **G** Average number of reads per nucleus. **H** Fraction of reads in peak regions
950 per dataset. All data are represented as mean \pm SD.

951

952 **Figure S2. Marker plots for cluster annotation and expression profiling of candidate**

953 **genes involved in SARS-CoV-2 cell entry. A** Dot plot of marker genes used for cluster
954 annotation. **B-D** Cell type specific gene expression of candidate genes for cell entry. Violin
955 plots display expression values per nucleus for genes encoding **B** Cathepsin L (*CTSL*),
956 **C** *FURIN* (*FURIN*) and **D** Basigin (*BSG*, CD147). **E** Correlation of *ACE2*⁺ and *TMPRSS2*⁺
957 AT2 cells with linear regression. **F, G** Fraction of AT2 cells with expression of *ACE2* and
958 *TMPRSS2* at each time point. Data are the same as Fig. 1D, E, but with potential outlier
959 sample D062 removed. * $p < 0.05$ (One-way ANOVA with post-hoc Tukey test).

960

961 **Figure S3. Expression analysis of viral entry genes.** Displayed are violin plots of

962 expression levels for entry genes related to other viruses including SARS-CoV, MERS,
963 coronavirus associated with common cold, Rhinovirus, Respiratory Syncytial Virus (RSV),
964 Adenovirus, Influenza Virus.

965

966 **Figure S4. Integrative analysis of *ACE2* and *TMPRSS2* expression in lungs from**
967 **aged individuals. A** Seurat3 Standard Integration (Stuart et al., 2019) was applied to

968 snRNA-seq data for 9 donors generated as part of this study and publicly available
969 scRNA-seq datasets 4 additional donor lungs (age > 55). AT2 cells from 13 donors were
970 clustered together via Louvain clustering with minimal batch variation. Left panel: t-SNE
971 visualization of cells colored by major cell type annotation. Epi other: predicted non-AT2

972 epithelial cells. Right panel: t-SNE visualization of cells colored by donor information. **B**
973 Normalized expression frequency of *ACE2* (left) and *TMPRSS2* (right) in AT2 cells. p
974 value was calculated using one-tailed t-test comparing normalized frequency in donors of
975 30yo group and aged group.

976

977 **Figure S5. Marker plots for cluster annotation of snATAC-seq and profiling of peaks**
978 **at candidate genes for SARS-CoV-2 cell entry. A** Dot plot of marker genes used for
979 cluster annotation. **B-D** Cell type resolved chromatin accessibility at peaks within +/- 650
980 kb of candidate genes for cell entry. Displayed are data for **B** *FURIN* (*FURIN*) and **C**
981 *Basigin* (*BSG*, CD147) **D** *Cathepsin L* (*CTSL*). Values are displayed as row normalized
982 proportion of cells with a fragment in a peak region. Black asterisks denote co-
983 accessibility from Cicero >0.05 (Cusanovich et al., 2018).

984

985 **Figure S6. Quantification of peaks with increased accessibility with age at tested**
986 **loci and donor resolved activity of sites not increased at *TMPRSS2* locus. A** Number
987 of peaks within +/- 650 kb of candidate genes for cell entry overlapping cIII and cIV from
988 Figure 3B. **B** Number of peaks co-accessible with the promoter of candidate genes for
989 cell entry overlapping cIII and cIV from Figure 3B. **C** Donor resolved analysis of 24/37
990 peaks at the *TMPRSS2* gene locus. Red asterisks denote FDR <0.05 (EdgeR) and black
991 asterisks denote p < 0.05 via t-test.

992

993

994

995 **SUPPLEMENTARY TABLE LEGENDS**

996 **Supplementary Table 1. Donor metadata tables.** Sheet 1: 30wk^{GA} - 30yo: Donor ID,
997 age, sex, race, clinical pathology diagnosis (clinPathDx), gestational age, overall quality
998 of the lung tissue assessment, type of death and cause of death were listed. Not shown
999 are data on body weight, body height, total lung weight and radial alveolar count
1000 assessment of alveolarization. All were all within normal limits for age. Abbreviations:
1001 DCD: donor after cardiac death; DBD: donor after brain death; GA: gestational age;
1002 RDS: respiratory distress syndrome. Sheet 2: aged cohort: Donor ID, age, sex, smoking
1003 history, race and cause of death were listed (Morse et al., 2019; Reyfman et al., 2019).

1004

1005 **Supplementary Table 2.** Cluster composition and number and fraction of nuclei
1006 expressing candidate for SARS-CoV2 cell entry.

1007

1008 **Supplementary Table 3.** Differential expressed analysis between *ACE2*⁺ and *ACE2*⁻ as
1009 well as *TMPRSS2*⁺ and *TMPRSS2*⁻ AT2 cells.

1010

1011 **Supplementary Table 4.** Annotation of peaks within a window of +/- 650 kb of
1012 candidate genes for SARS-CoV2 cell entry.

1013

1014 **Supplementary Table 5.** Annotation of peaks co-accessible with candidate genes for
1015 SARS-CoV2 cell entry and age-associated changes of chromatin accessibility of peaks
1016 co-accessible with *TMPRSS2* promoter.

1017

1018 **Supplementary Table 6.** GREAT analysis of peaks increasing with age in AT2 cells
1019 (groups cIII and cIV in Fig 3B).

1020

1021 **Supplementary Table 7.** *De novo* motif enrichment analysis of peaks increasing with
1022 age in AT2 cells (groups cIII and cIV in Fig 3B).

1023

1024 **Supplementary Table 8.** Indexes and primer sequences for snATAC-seq libraries.

1025 **REFERENCES**

- 1026 Aguet, F., Barbeira, A.N., Bonazzola, R., Brown, A., Castel, S.E., Jo, B., Kasela, S., Kim-
1027 Hellmuth, S., Liang, Y., Oliva, M., *et al.* (2019). The GTEx Consortium atlas of genetic
1028 regulatory effects across human tissues. bioRxiv.
- 1029 Ardini-Poleske, M.E., Clark, R.F., Ansong, C., Carson, J.P., Corley, R.A., Deutsch, G.H.,
1030 Hagood, J.S., Kaminski, N., Mariani, T.J., Potter, S.S., *et al.* (2017). LungMAP: The
1031 Molecular Atlas of Lung Development Program. *Am J Physiol Lung Cell Mol Physiol*
1032 *313*, L733-L740.
- 1033 Bandyopadhyay, G., Huyck, H.L., Misra, R.S., Bhattacharya, S., Wang, Q., Mereness, J.,
1034 Lillis, J., Myers, J.R., Ashton, J., Bushnell, T., *et al.* (2018). Dissociation, cellular
1035 isolation, and initial molecular characterization of neonatal and pediatric human lung
1036 tissues. *Am J Physiol Lung Cell Mol Physiol* *315*, L576-L583.
- 1037 Battles, M.B., and McLellan, J.S. (2019). Respiratory syncytial virus entry and how to
1038 block it. *Nat Rev Microbiol* *17*, 233-245.
- 1039 Bi, Q., Wu, Y., Mei, S., Ye, C., Zou, X., Zhang, Z., Liu, X., Wei, L., Truelove, S.A., Zhang,
1040 T., *et al.* (2020). Epidemiology and Transmission of COVID-19 in Shenzhen China:
1041 Analysis of 391 cases and 1,286 of their close contacts. medRxiv.
- 1042 Bochkov, Y.A., and Gern, J.E. (2016). Rhinoviruses and Their Receptors: Implications for
1043 Allergic Disease. *Curr Allergy Asthma Rep* *16*, 30.
- 1044 Buenrostro, J.D., Giresi, P.G., Zaba, L.C., Chang, H.Y., and Greenleaf, W.J. (2013).
1045 Transposition of native chromatin for fast and sensitive epigenomic profiling of open
1046 chromatin, DNA-binding proteins and nucleosome position. *Nat Methods* *10*, 1213-
1047 1218.
- 1048 Buenrostro, J.D., Wu, B., Litzenburger, U.M., Ruff, D., Gonzales, M.L., Snyder, M.P.,
1049 Chang, H.Y., and Greenleaf, W.J. (2015). Single-cell chromatin accessibility reveals
1050 principles of regulatory variation. *Nature* *523*, 486-490.
- 1051 CDC, C.-R.T. (2020). Coronavirus Disease 2019 in Children — United States, February
1052 12–April 2, 2020. *MMWR Morb Mortal Wkly Rep* *2020* *69*, 422–426.
- 1053 Chen, X., Miragaia, R.J., Natarajan, K.N., and Teichmann, S.A. (2018). A rapid and robust
1054 method for single cell chromatin accessibility profiling. *Nat Commun* *9*, 5345.
- 1055 Chen, Z., Mi, L., Xu, J., Yu, J., Wang, X., Jiang, J., Xing, J., Shang, P., Qian, A., Li, Y., *et*
1056 *al.* (2005). Function of HAb18G/CD147 in invasion of host cells by severe acute
1057 respiratory syndrome coronavirus. *J Infect Dis* *191*, 755-760.
- 1058 Chiou, J., Zeng, C., Cheng, Z., Han, J.Y., Schlichting, M., Huang, S., Wang, J., Sui, Y.,
1059 Deogaygay, A., Okino, M.-L., *et al.* (2019). Single cell chromatin accessibility reveals
1060 pancreatic islet cell type- and state-specific regulatory programs of diabetes risk.
1061 bioRxiv.
- 1062 Consortium, E.P. (2012). An integrated encyclopedia of DNA elements in the human
1063 genome. *Nature* *489*, 57-74.
- 1064 Corces, M.R., Shcherbina, A., Kundu, S., Gloudemans, M.J., Frésard, L., Granja, J.M.,
1065 Louie, B.H., Shams, S., Bagdatli, S.T., Mumbach, M.R., *et al.* (2020). Single-cell
1066 epigenomic identification of inherited risk loci in Alzheimer’s and Parkinson’s disease.
1067 bioRxiv.
- 1068 Corces, M.R., Trevino, A.E., Hamilton, E.G., Greenside, P.G., Sinnott-Armstrong, N.A.,
1069 Vesuna, S., Satpathy, A.T., Rubin, A.J., Montine, K.S., Wu, B., *et al.* (2017). An

- 1070 improved ATAC-seq protocol reduces background and enables interrogation of frozen
1071 tissues. *Nat Methods* 14, 959-962.
- 1072 Coutard, B., Valle, C., de Lamballerie, X., Canard, B., Seidah, N.G., and Decroly, E.
1073 (2020). The spike glycoprotein of the new coronavirus 2019-nCoV contains a furin-
1074 like cleavage site absent in CoV of the same clade. *Antiviral Res* 176, 104742.
- 1075 Cusanovich, D.A., Daza, R., Adey, A., Pliner, H.A., Christiansen, L., Gunderson, K.L.,
1076 Steemers, F.J., Trapnell, C., and Shendure, J. (2015). Multiplex single cell profiling of
1077 chromatin accessibility by combinatorial cellular indexing. *Science* 348, 910-914.
- 1078 Cusanovich, D.A., Hill, A.J., Aghamirzaie, D., Daza, R.M., Pliner, H.A., Berletch, J.B.,
1079 Filippova, G.N., Huang, X., Christiansen, L., DeWitt, W.S., *et al.* (2018). A Single-Cell
1080 Atlas of In Vivo Mammalian Chromatin Accessibility. *Cell* 174, 1309-1324 e1318.
- 1081 Du, Y., Tu, L., Zhu, P., Mu, M., Wang, R., Yang, P., Wang, X., Hu, C., Ping, R., Hu, P., *et*
1082 *al.* (2020). Clinical Features of 85 Fatal Cases of COVID-19 from Wuhan: A
1083 Retrospective Observational Study. *Am J Respir Crit Care Med*.
- 1084 Fang, R., Preissl, S., Hou, X., Lucero, J., Wang, X., Motamedi, A., Shiau, A.K., Mukamel,
1085 E.A., Zhang, Y., Behrens, M.M., *et al.* (2019). Fast and Accurate Clustering of Single
1086 Cell Epigenomes Reveals *Cis*-Regulatory Elements in Rare Cell Types.
1087 bioRxiv.
- 1088 Fornes, O., Castro-Mondragon, J.A., Khan, A., van der Lee, R., Zhang, X., Richmond,
1089 P.A., Modi, B.P., Correard, S., Gheorghe, M., Baranasic, D., *et al.* (2020). JASPAR
1090 2020: update of the open-access database of transcription factor binding profiles.
1091 *Nucleic Acids Res* 48, D87-D92.
- 1092 Grant, C.E., Bailey, T.L., and Noble, W.S. (2011). FIMO: scanning for occurrences of a
1093 given motif. *Bioinformatics* 27, 1017-1018.
- 1094 Heinz, S., Benner, C., Spann, N., Bertolino, E., Lin, Y.C., Laslo, P., Cheng, J.X., Murre,
1095 C., Singh, H., and Glass, C.K. (2010). Simple combinations of lineage-determining
1096 transcription factors prime cis-regulatory elements required for macrophage and B cell
1097 identities. *Mol Cell* 38, 576-589.
- 1098 Huang, I.C., Bosch, B.J., Li, W., Farzan, M., Rottier, P.M., and Choe, H. (2006). SARS-
1099 CoV, but not HCoV-NL63, utilizes cathepsins to infect cells: viral entry. *Adv Exp Med*
1100 *Biol* 581, 335-338.
- 1101 Imai, Y., Kuba, K., Rao, S., Huan, Y., Guo, F., Guan, B., Yang, P., Sarao, R., Wada, T.,
1102 Leong-Poi, H., *et al.* (2005). Angiotensin-converting enzyme 2 protects from severe
1103 acute lung failure. *Nature* 436, 112-116.
- 1104 Iwata-Yoshikawa, N., Okamura, T., Shimizu, Y., Hasegawa, H., Takeda, M., and Nagata,
1105 N. (2019). TMPRSS2 Contributes to Virus Spread and Immunopathology in the
1106 Airways of Murine Models after Coronavirus Infection. *J Virol* 93.
- 1107 Karczewski, K.J., Francioli, L.C., Tiao, G., Cummings, B.B., Alföldi, J., Wang, Q., Collins,
1108 R.L., Laricchia, K.M., Ganna, A., Birnbaum, D.P., *et al.* (2019). Variation across
1109 141,456 human exomes and genomes reveals the spectrum of loss-of-function
1110 intolerance across human protein-coding genes. bioRxiv.
- 1111 Kim, T.S., Heinlein, C., Hackman, R.C., and Nelson, P.S. (2006). Phenotypic analysis of
1112 mice lacking the *Tmprss2*-encoded protease. *Mol Cell Biol* 26, 965-975.
- 1113 Korsunsky, I., Millard, N., Fan, J., Slowikowski, K., Zhang, F., Wei, K., Baglaenko, Y.,
1114 Brenner, M., Loh, P.R., and Raychaudhuri, S. (2019). Fast, sensitive and accurate
1115 integration of single-cell data with Harmony. *Nat Methods* 16, 1289-1296.

- 1116 Kuba, K., Imai, Y., Rao, S., Gao, H., Guo, F., Guan, B., Huan, Y., Yang, P., Zhang, Y.,
1117 Deng, W., *et al.* (2005). A crucial role of angiotensin converting enzyme 2 (ACE2) in
1118 SARS coronavirus-induced lung injury. *Nat Med* 11, 875-879.
- 1119 Lab, N. (2020). UK-Biobank.
- 1120 Lan, J., Ge, J., Yu, J., Shan, S., Zhou, H., Fan, S., Zhang, Q., Shi, X., Wang, Q., Zhang,
1121 L., *et al.* (2020). Structure of the SARS-CoV-2 spike receptor-binding domain bound
1122 to the ACE2 receptor. *Nature*.
- 1123 Laporte, M., and Naesens, L. (2017). Airway proteases: an emerging drug target for
1124 influenza and other respiratory virus infections. *Curr Opin Virol* 24, 16-24.
- 1125 Lareau, C.A., Duarte, F.M., Chew, J.G., Kartha, V.K., Burkett, Z.D., Kohlway, A.S.,
1126 Pokholok, D., Aryee, M.J., Steemers, F.J., Lebofsky, R., *et al.* (2019). Droplet-based
1127 combinatorial indexing for massive-scale single-cell chromatin accessibility. *Nat*
1128 *Biotechnol* 37, 916-924.
- 1129 Lee, D., Gorkin, D.U., Baker, M., Strober, B.J., Asoni, A.L., McCallion, A.S., and Beer,
1130 M.A. (2015). A method to predict the impact of regulatory variants from DNA
1131 sequence. *Nat Genet* 47, 955-961.
- 1132 Li, H., and Durbin, R. (2009). Fast and accurate short read alignment with Burrows-
1133 Wheeler transform. *Bioinformatics* 25, 1754-1760.
- 1134 Li, H., Handsaker, B., Wysoker, A., Fennell, T., Ruan, J., Homer, N., Marth, G., Abecasis,
1135 G., Durbin, R., and Genome Project Data Processing, S. (2009). The Sequence
1136 Alignment/Map format and SAMtools. *Bioinformatics* 25, 2078-2079.
- 1137 Limburg, H., Harbig, A., Bestle, D., Stein, D.A., Moulton, H.M., Jaeger, J., Janga, H.,
1138 Hards, K., Koepke, J., Schulte, L., *et al.* (2019). TMPRSS2 Is the Major Activating
1139 Protease of Influenza A Virus in Primary Human Airway Cells and Influenza B Virus in
1140 Human Type II Pneumocytes. *J Virol* 93.
- 1141 Lukhele, S., Boukhaled, G.M., and Brooks, D.G. (2019). Type I interferon signaling,
1142 regulation and gene stimulation in chronic virus infection. *Semin Immunol* 43, 101277.
- 1143 Matsuyama, S., Nao, N., Shirato, K., Kawase, M., Saito, S., Takayama, I., Nagata, N.,
1144 Sekizuka, T., Kato, H., Kato, F., *et al.* (2020). Enhanced isolation of SARS-CoV-2 by
1145 TMPRSS2-expressing cells. *Proc Natl Acad Sci U S A* 117, 7001-7003.
- 1146 Maurano, M.T., Haugen, E., Sandstrom, R., Vierstra, J., Shafer, A., Kaul, R., and
1147 Stamatoyannopoulos, J.A. (2015). Large-scale identification of sequence variants
1148 influencing human transcription factor occupancy in vivo. *Nat Genet* 47, 1393-1401.
- 1149 McGinnis, C.S., Murrow, L.M., and Gartner, Z.J. (2019). DoubletFinder: Doublet Detection
1150 in Single-Cell RNA Sequencing Data Using Artificial Nearest Neighbors. *Cell Syst* 8,
1151 329-337 e324.
- 1152 McLean, C.Y., Bristor, D., Hiller, M., Clarke, S.L., Schaar, B.T., Lowe, C.B., Wenger, A.M.,
1153 and Bejerano, G. (2010). GREAT improves functional interpretation of cis-regulatory
1154 regions. *Nat Biotechnol* 28, 495-501.
- 1155 Mesev, E.V., LeDesma, R.A., and Ploss, A. (2019). Decoding type I and III interferon
1156 signalling during viral infection. *Nat Microbiol* 4, 914-924.
- 1157 Morse, C., Tabib, T., Sembrat, J., Buschur, K.L., Bittar, H.T., Valenzi, E., Jiang, Y., Kass,
1158 D.J., Gibson, K., Chen, W., *et al.* (2019). Proliferating SPP1/MERTK-expressing
1159 macrophages in idiopathic pulmonary fibrosis. *Eur Respir J* 54.
- 1160 Narayanan, M., Owers-Bradley, J., Beardsmore, C.S., Mada, M., Ball, I., Garipov, R.,
1161 Panesar, K.S., Kuehni, C.E., Spycher, B.D., Williams, S.E., *et al.* (2012).

- 1162 Alveolarization continues during childhood and adolescence: new evidence from
1163 helium-3 magnetic resonance. *Am J Respir Crit Care Med* **185**, 186-191.
- 1164 Ochs, M., Nyengaard, J.R., Jung, A., Knudsen, L., Voigt, M., Wahlers, T., Richter, J., and
1165 Gundersen, H.J. (2004). The number of alveoli in the human lung. *Am J Respir Crit*
1166 *Care Med* **169**, 120-124.
- 1167 Oki, S., Ohta, T., Shioi, G., Hatanaka, H., Ogasawara, O., Okuda, Y., Kawaji, H., Nakaki,
1168 R., Sese, J., and Meno, C. (2018). ChIP-Atlas: a data-mining suite powered by full
1169 integration of public ChIP-seq data. *EMBO Rep* **19**.
- 1170 Peck, K.M., Burch, C.L., Heise, M.T., and Baric, R.S. (2015). Coronavirus Host Range
1171 Expansion and Middle East Respiratory Syndrome Coronavirus Emergence:
1172 Biochemical Mechanisms and Evolutionary Perspectives. *Annu Rev Virol* **2**, 95-117.
- 1173 Pickrell, J.K. (2014). Joint analysis of functional genomic data and genome-wide
1174 association studies of 18 human traits. *Am J Hum Genet* **94**, 559-573.
- 1175 Pliner, H.A., Packer, J.S., McFaline-Figueroa, J.L., Cusanovich, D.A., Daza, R.M.,
1176 Aghamirzaie, D., Srivatsan, S., Qiu, X., Jackson, D., Minkina, A., *et al.* (2018). Cicero
1177 Predicts cis-Regulatory DNA Interactions from Single-Cell Chromatin Accessibility
1178 Data. *Mol Cell* **71**, 858-871 e858.
- 1179 Preissl, S., Fang, R., Huang, H., Zhao, Y., Raviram, R., Gorkin, D.U., Zhang, Y., Sos,
1180 B.C., Afzal, V., Dickel, D.E., *et al.* (2018). Single-nucleus analysis of accessible
1181 chromatin in developing mouse forebrain reveals cell-type-specific transcriptional
1182 regulation. *Nat Neurosci* **21**, 432-439.
- 1183 Qi, F., Qian, S., Zhang, S., and Zhang, Z. (2020). Single cell RNA sequencing of 13
1184 human tissues identify cell types and receptors of human coronaviruses. *bioRxiv*.
- 1185 Raj, V.S., Mou, H., Smits, S.L., Dekkers, D.H., Muller, M.A., Dijkman, R., Muth, D.,
1186 Demmers, J.A., Zaki, A., Fouchier, R.A., *et al.* (2013). Dipeptidyl peptidase 4 is a
1187 functional receptor for the emerging human coronavirus-EMC. *Nature* **495**, 251-254.
- 1188 Reinke, L.M., Spiegel, M., Plegge, T., Hartleib, A., Nehlmeier, I., Gierer, S., Hoffmann,
1189 M., Hofmann-Winkler, H., Winkler, M., and Pöhlmann, S. (2017). Different residues in
1190 the SARS-CoV spike protein determine cleavage and activation by the host cell
1191 protease TMPRSS2. *PLoS One* **12**, e0179177.
- 1192 Reyfman, P.A., Walter, J.M., Joshi, N., Anekalla, K.R., McQuattie-Pimentel, A.C., Chiu,
1193 S., Fernandez, R., Akbarpour, M., Chen, C.I., Ren, Z., *et al.* (2019). Single-Cell
1194 Transcriptomic Analysis of Human Lung Provides Insights into the Pathobiology of
1195 Pulmonary Fibrosis. *Am J Respir Crit Care Med* **199**, 1517-1536.
- 1196 Roadmap Epigenomics, C., Kundaje, A., Meuleman, W., Ernst, J., Bilenky, M., Yen, A.,
1197 Heravi-Moussavi, A., Kheradpour, P., Zhang, Z., Wang, J., *et al.* (2015). Integrative
1198 analysis of 111 reference human epigenomes. *Nature* **518**, 317-330.
- 1199 Robinson, M.D., McCarthy, D.J., and Smyth, G.K. (2010). edgeR: a Bioconductor
1200 package for differential expression analysis of digital gene expression data.
1201 *Bioinformatics* **26**, 139-140.
- 1202 Satpathy, A.T., Granja, J.M., Yost, K.E., Qi, Y., Meschi, F., McDermott, G.P., Olsen, B.N.,
1203 Mumbach, M.R., Pierce, S.E., Corces, M.R., *et al.* (2019). Massively parallel single-
1204 cell chromatin landscapes of human immune cell development and intratumoral T cell
1205 exhaustion. *Nat Biotechnol* **37**, 925-936.
- 1206 Schiller, H.B., Montoro, D.T., Simon, L.M., Rawlins, E.L., Meyer, K.B., Strunz, M., Vieira
1207 Braga, F.A., Timens, W., Koppelman, G.H., Budinger, G.R.S., *et al.* (2019). The

- 1208 Human Lung Cell Atlas: A High-Resolution Reference Map of the Human Lung in
1209 Health and Disease. *Am J Respir Cell Mol Biol* 61, 31-41.
- 1210 Stuart, T., Butler, A., Hoffman, P., Hafemeister, C., Papalexi, E., Mauck, W.M., 3rd, Hao,
1211 Y., Stoeckius, M., Smibert, P., and Satija, R. (2019). Comprehensive Integration of
1212 Single-Cell Data. *Cell* 177, 1888-1902 e1821.
- 1213 Sudlow, C., Gallacher, J., Allen, N., Beral, V., Burton, P., Danesh, J., Downey, P., Elliott,
1214 P., Green, J., Landray, M., *et al.* (2015). UK biobank: an open access resource for
1215 identifying the causes of a wide range of complex diseases of middle and old age.
1216 *PLoS Med* 12, e1001779.
- 1217 Thurman, R.E., Rynes, E., Humbert, R., Vierstra, J., Maurano, M.T., Haugen, E.,
1218 Sheffield, N.C., Stergachis, A.B., Wang, H., Vernot, B., *et al.* (2012). The accessible
1219 chromatin landscape of the human genome. *Nature* 489, 75-82.
- 1220 Traag, V.A., Waltman, L., and van Eck, N.J. (2019). From Louvain to Leiden:
1221 guaranteeing well-connected communities. *Sci Rep* 9, 5233.
- 1222 Travaglini, K.J., Nabhan, A.N., Penland, L., Sinha, R., Gillich, A., Sit, R.V., Chang, S.,
1223 Conley, S.D., Mori, Y., Seita, J., *et al.* (2020). A molecular cell atlas of the human lung
1224 from single cell RNA sequencing. *bioRxiv*.
- 1225 Tyner, C., Barber, G.P., Casper, J., Clawson, H., Diekhans, M., Eisenhart, C., Fischer,
1226 C.M., Gibson, D., Gonzalez, J.N., Guruvadoo, L., *et al.* (2017). The UCSC Genome
1227 Browser database: 2017 update. *Nucleic Acids Res* 45, D626-D634.
- 1228 Walls, A.C., Park, Y.J., Tortorici, M.A., Wall, A., McGuire, A.T., and Velesler, D. (2020).
1229 Structure, Function, and Antigenicity of the SARS-CoV-2 Spike Glycoprotein. *Cell*.
- 1230 Wang, M., Wu, Q., Xu, W., Qiao, B., Wang, J., Zheng, H., Jiang, S., Mei, J., Wu, Z., Deng,
1231 Y., *et al.* (2020). Clinical diagnosis of 8274 samples with 2019-novel coronavirus in
1232 Wuhan. *medRxiv*.
- 1233 Wang, X., Park, J., Susztak, K., Zhang, N.R., and Li, M. (2019). Bulk tissue cell type
1234 deconvolution with multi-subject single-cell expression reference. *Nat Commun* 10,
1235 380.
- 1236 Waradon Sungnak, N.H., Christophe Bécavin, Marijn Berg, HCA Lung Biological Network
1237 (2020). SARS-CoV-2 Entry Genes Are Most Highly Expressed in Nasal Goblet and
1238 Ciliated Cells within Human Airways. *arXiv*.
- 1239 Wolf, F.A., Angerer, P., and Theis, F.J. (2018). SCANPY: large-scale single-cell gene
1240 expression data analysis. *Genome Biol* 19, 15.
- 1241 Wu, X., Cai, Y., Huang, X., Yu, X., Zhao, L., Wang, F., Li, Q., Gu, S., Xu, T., Li, Y., *et al.*
1242 (2020). Co-infection with SARS-CoV-2 and Influenza A Virus in Patient with
1243 Pneumonia, China. *Emerg Infect Dis* 26.
- 1244 Xia, C., Anderson, P., and Hahm, B. (2018). Viral dedication to vigorous destruction of
1245 interferon receptors. *Virology* 522, 19-26.
- 1246 Xu, Y., Mizuno, T., Sridharan, A., Du, Y., Guo, M., Tang, J., Wikenheiser-Brokamp, K.A.,
1247 Perl, A.T., Funari, V.A., Gokey, J.J., *et al.* (2016). Single-cell RNA sequencing
1248 identifies diverse roles of epithelial cells in idiopathic pulmonary fibrosis. *JCI Insight* 1,
1249 e90558.
- 1250 Yan, R., Zhang, Y., Li, Y., Xia, L., Guo, Y., and Zhou, Q. (2020). Structural basis for the
1251 recognition of SARS-CoV-2 by full-length human ACE2. *Science* 367, 1444-1448.

- 1252 Yeager, C.L., Ashmun, R.A., Williams, R.K., Cardellichio, C.B., Shapiro, L.H., Look, A.T.,
1253 and Holmes, K.V. (1992). Human aminopeptidase N is a receptor for human
1254 coronavirus 229E. *Nature* 357, 420-422.
- 1255 Zhang, Y., Liu, T., Meyer, C.A., Eeckhoute, J., Johnson, D.S., Bernstein, B.E., Nusbaum,
1256 C., Myers, R.M., Brown, M., Li, W., *et al.* (2008). Model-based analysis of ChIP-Seq
1257 (MACS). *Genome Biol* 9, R137.
- 1258 Zhao, Y., Zhao, Z., Wang, Y., Zhou, Y., Ma, Y., and Zuo, W. (2020). Single-cell RNA
1259 expression profiling of ACE2, the receptor of SARS-CoV-2. *bioRxiv*.
- 1260 Zheng, G.X., Terry, J.M., Belgrader, P., Ryvkin, P., Bent, Z.W., Wilson, R., Ziraldo, S.B.,
1261 Wheeler, T.D., McDermott, G.P., Zhu, J., *et al.* (2017). Massively parallel digital
1262 transcriptional profiling of single cells. *Nat Commun* 8, 14049.
- 1263 Zhou, N., Pan, T., Zhang, J., Li, Q., Zhang, X., Bai, C., Huang, F., Peng, T., Liu, C., Tao,
1264 L., *et al.* (2016). Glycopeptide Antibiotics Potently Inhibit Cathepsin L in the Late
1265 Endosome/Lysosome and Block the Entry of Ebola Virus, Middle East Respiratory
1266 Syndrome Coronavirus (MERS-CoV), and Severe Acute Respiratory Syndrome
1267 Coronavirus (SARS-CoV). *J Biol Chem* 291, 9218-9232.
- 1268 Zhou, X., Zhu, L., Lizarraga, R., and Chen, Y. (2017). Human Airway Epithelial Cells
1269 Direct Significant Rhinovirus Replication in Monocytic Cells by Enhancing ICAM1
1270 Expression. *Am J Respir Cell Mol Biol* 57, 216-225.
- 1271 Ziegler, C.a.A., Samuel J. and Nyquist, Sarah K. and Mbano, Ian and Miao, Vincent N.
1272 and Cao, Yuming and Yousif, Ashraf S. and Bals, Julia and Hauser, Blake M. and
1273 Feldman, Jared and Muus, Christoph and Wadsworth II, Marc H. and Kazer, Samuel
1274 and Hughes, Travis K. and Doran, Benjamin and Gatter, G. James and Vukovic,
1275 Marko and Tzouanas, Constantine N. and Taliaferro, Faith and Guo, Zhiru and Wang,
1276 Jennifer P. and Dwyer, Daniel F. and Buchheit, Kathleen M. and Boyce, Joshua and
1277 Barrett, Nora A. and Laidlaw, Tanya M. and Carroll, Shaina L. and Colonna, Lucrezia
1278 and Tkachev, Victor and Yu, Alison and Zheng, Henqi Betty and Gideon, Hannah P.
1279 and Winchell, Caylin G. and Lin, Philana L. and Berger, Bonnie and Leslie, Alasdair
1280 and Flynn, JoAnne L. and Fortune, Sarah M. and Finberg, Robert W. and Kean, Leslie
1281 and Garber, Manuel and Schmidt, Aaron and Lingwood, Daniel and Shalek, Alex K.
1282 and Ordovas-Montanes, Jose and Lung Biological Network, HCA (2020). SARS-CoV-
1283 2 Receptor ACE2 is an Interferon-Stimulated Gene in Human Airway Epithelial Cells
1284 and Is Enriched in Specific Cell Subsets Across Tissues. *Cell*.
- 1285 Zou, X., Chen, K., Zou, J., Han, P., Hao, J., and Han, Z. (2020). Single-cell RNA-seq data
1286 analysis on the receptor ACE2 expression reveals the potential risk of different human
1287 organs vulnerable to 2019-nCoV infection. *Front Med*.

1288

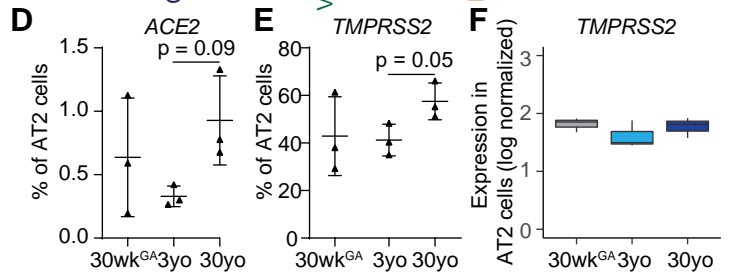
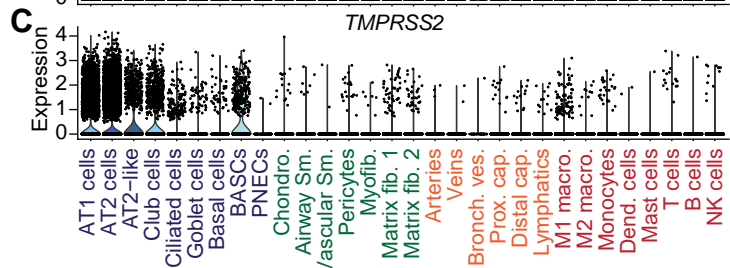
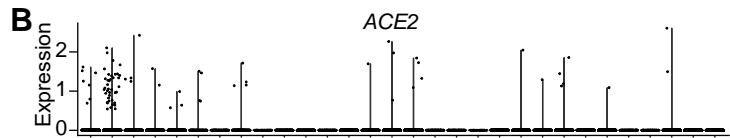
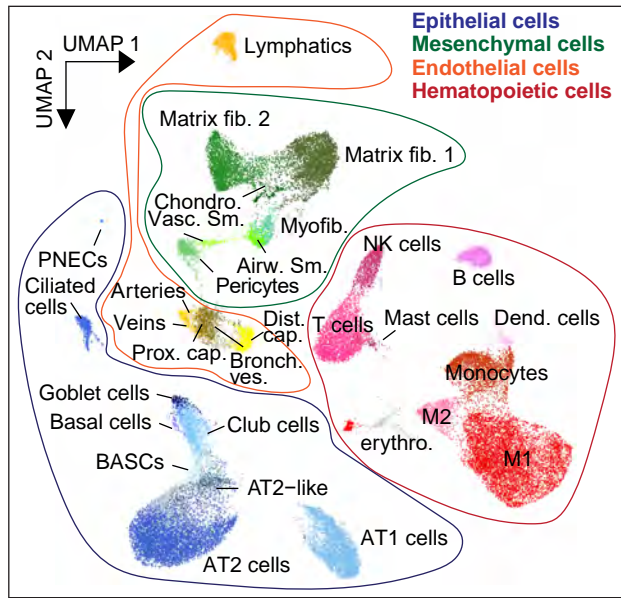
Figure 1**A** Human Lung snRNA-seq (46,500 nuclei)

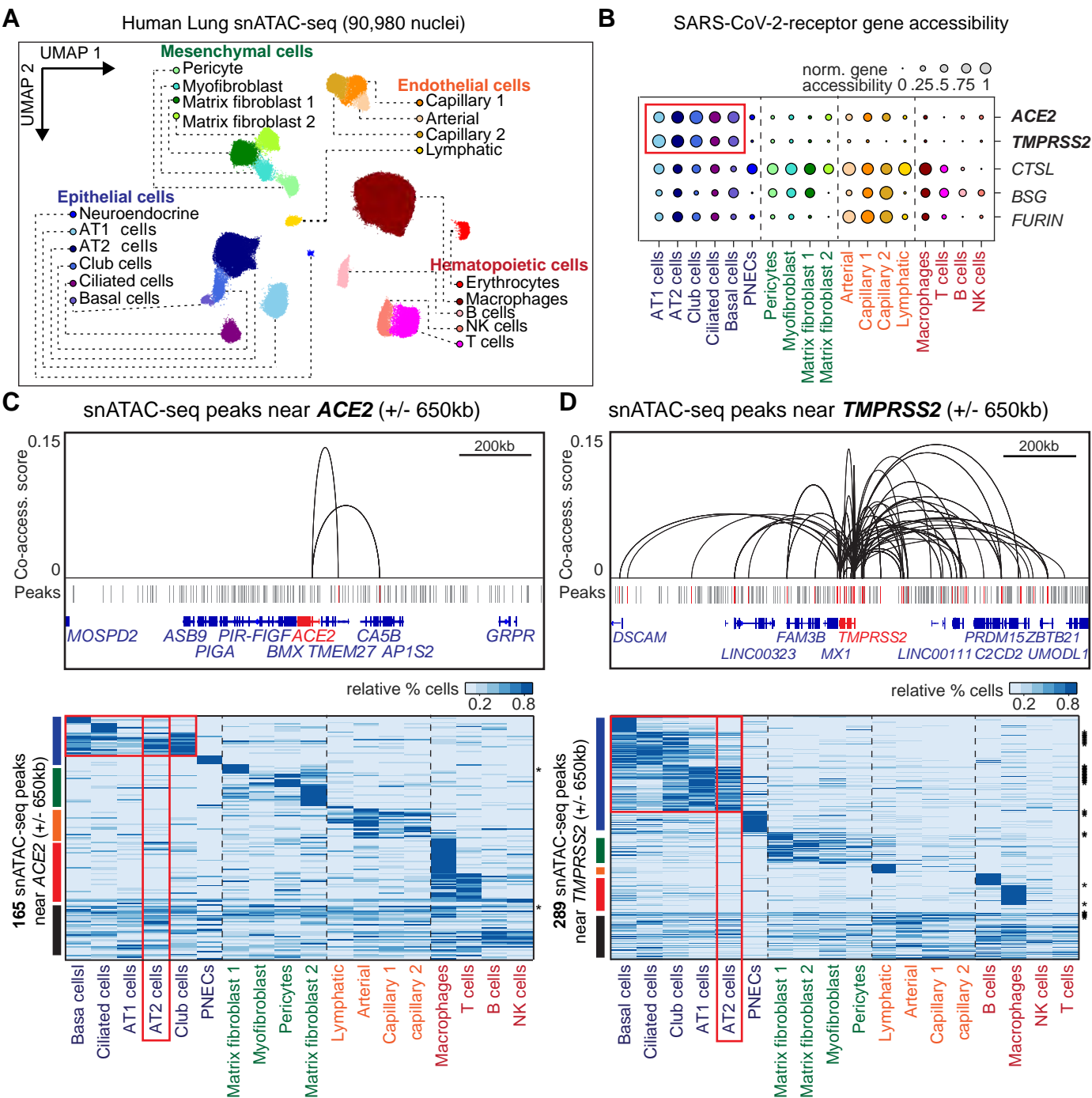
Figure 2

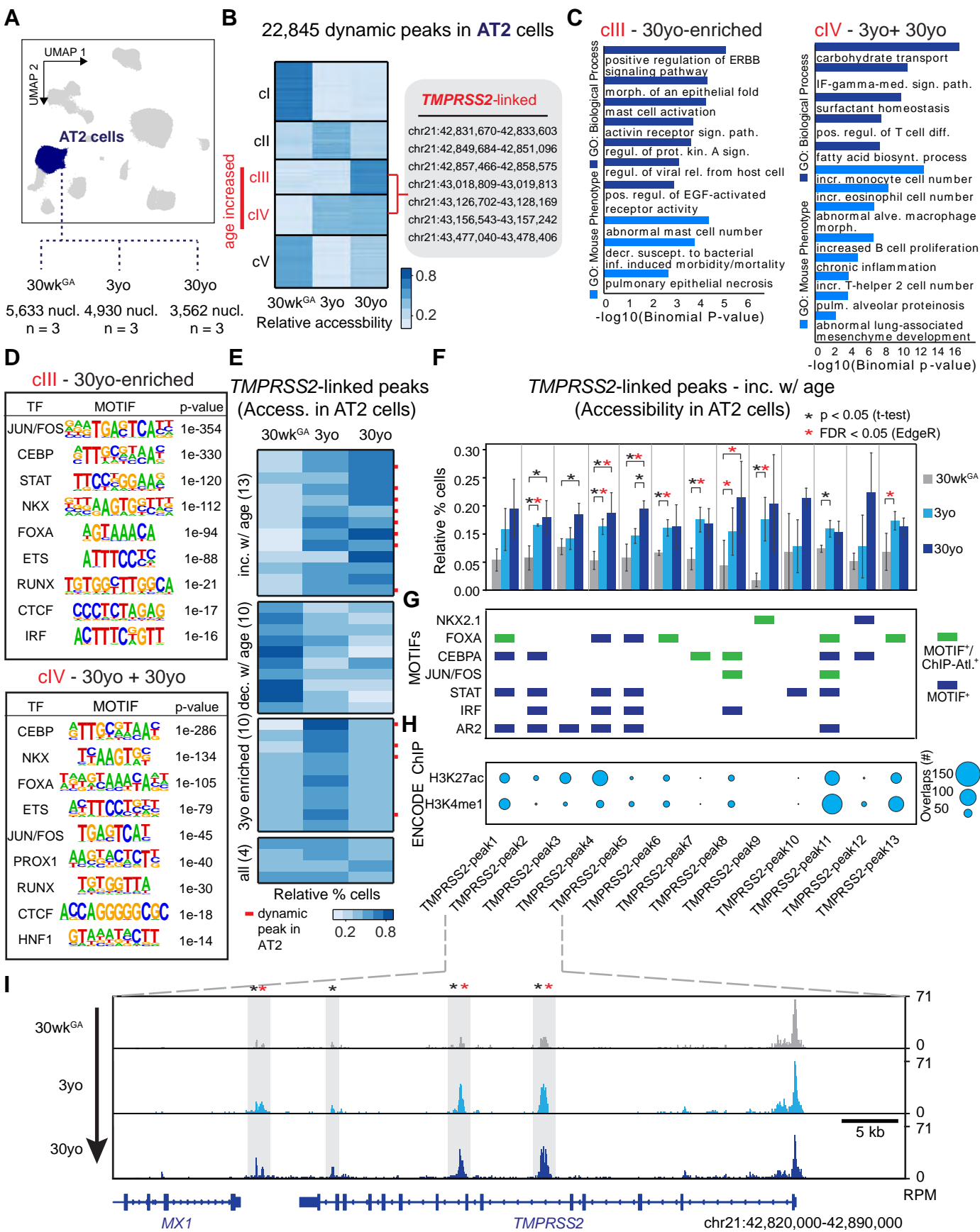
Figure 3

Figure 4

